Seasonal and inter-annual variability of ~~carbon~~CO$_2$ fluxes in southern Africa seen by GOSAT

Eva-Marie Metz[1], Sanam Noreen Vardag[1,2], Sourish Basu[3,4], Martin Jung[5], André Butz[1,2,6]

[1]Institute of Environmental Physics, Heidelberg University, Heidelberg, 69120, Germany
[2]Heidelberg Center for the Environment (HCE), Heidelberg University, Heidelberg, 69120, Germany.
[3]Goddard Space Flight Center, NASA, Greenbelt, MD 20771, USA
[4]Earth System Science Interdisciplinary Center, University of Maryland, College Park, MD 20740, USA
[5]Max Planck Institute for Biogeochemistry, Jena, 07745, Germany
[6]Interdisciplinary Center for Scientific Computing (IWR), Heidelberg University, Heidelberg, 69120, Germany

Correspondence to: Eva-Marie Metz (eva-marie.metz@iup.uni-heidelberg.de)

Abstract. The inter-annual variability of the global carbon sink is heavily influenced by semi-arid regions. Southern hemispheric Africa has large semi-arid and arid regions. However, there is only a sparse coverage of in situ CO$_2$ measurements on the southern hemisphere. This leads to uncertainties in measurement-based carbon flux estimates for these regions. Also, dynamic global vegetation models (DGVMs) show large inconsistencies in semi-arid regions. Satellite CO$_2$ measurements offer a spatially extensive and independent source of information about the southern African carbon cycle. We examine Greenhouse Gases Observing Satellite (GOSAT) CO$_2$ concentration measurements from 2009 to 2018 in southern Africa. We infer CO$_2$ land-atmosphere fluxes which are consistent with the GOSAT measurements using the atmospheric inversion system TM5-4DVar. We find systematic differences between ~~these satellite based carbon fluxes and~~ atmospheric inversions ~~based~~performed on satellite observations versus inversions that assimilate only in situ measurements ~~pointing towards a~~. This suggests limited measurement information content in the latter. We use the GOSAT based fluxes and additionally Solar Induced Fluorescence (SIF), a proxy for photosynthesis, as atmospheric constraints to select DGVMs of the TRENDYv9 ensemble which show compatible fluxes. The selected DGVMs allow for studying the vegetation processes driving the southern African carbon cycle. ~~We show that the variability of~~Doing so, our satellite-based process analyses pinpoint photosynthetic uptake ~~mainly drives~~in the southern grasslands to be the main driver of the inter-annual variability of the southern African carbon fluxes~~. The~~, agreeing with former studies based on vegetation models alone. We find that the seasonal cycle, however, is substantially influenced by enhanced soil respiration due to soil rewetting at the beginning of the rainy season. The latter result emphasizes the importance of correctly representing the response of semi-arid ecosystems to soil rewetting in DGVMs.

1 Introduction

The terrestrial carbon sink currently takes up nearly one third of human made greenhouse gases and thereby ~~slows down~~mitigates climate change (Friedlingstein et al., 2023). The amount of CO$_2$ taken up by global ecosystems varies

substantially from year to year. This inter-annual variability (IAV) reflects the response of ecosystem carbon uptake to varying climate conditions such as temperature or precipitation fluctuations (Zeng et al., 2005; Zhang et al., 2018; Piao et al., 2020). Current vegetation models struggle in accurately reproducing IAV of the terrestrial carbon sink and an imbalance exists between the modelled and measured total global sink estimates (Friedlingstein et al., 2023). The imbalance is even stronger when examining carbon fluxes on smaller spatial scales (Bastos et al., 2020) and implies that there is still an insufficient understanding of the terrestrial processes driving land carbon exchange. A better understanding is needed to improve climate models and climate change predictions (Steiner et al., 2020).

Semi-arid regions contribute substantially to the IAV of the global terrestrial carbon sink. In these regions, precipitation and temperature fluctuations heavily impact the IAV of carbon fluxes (Poulter et al., 2014; Ahlström et al., 2015). Africa has large areas of semi-arid and arid ecosystems (Williams et al., 2007) and contributes substantially to the global IAV (Williams et al., 2007; Valentini et al., 2014; Pan et al., 2020). However, in situ CO_2 measurements in Africa are very sparse leading to large uncertainties in carbon flux estimates from atmospheric inversions and machine learning approaches (Valentini et al., 2014; Ernst et al., 2024). Dynamic Global Vegetation Models (DGVMs), also, show large inconsistencies amongst each other and tend to underestimate the inter-annual CO_2 flux variability in semi-arid regions (MacBean et al., 2021).

Satellite CO_2 concentration measurements, for example from the Greenhouse Gases Observing Satellite (GOSAT) measuring CO_2 concentrations since 2009 or the Orbiting Carbon Observatory-2 (OCO-2) launched in 2014, have much denser coverage compared to in situ measurements. Previous studies found systematic differences between satellite- and in situ measurement-based CO_2 concentrations and fluxes in southern Africa (Mengistu and Mengistu Tsidu, 2020; ~~Taylor et al., 2022;~~ Byrne et al., 2023). Byrne et al. (2023) attribute these differences mainly to the sparse coverage of in situ CO_2 measurements. The studies emphasize the potential of satellite-based atmospheric inversions to provide additional information and therefore more robust estimates of the carbon fluxes in southern hemispheric Africa, which then enable research about processes driving the CO_2 exchange. Metz et al. (2023) demonstrate the potential of combining satellite-based CO_2 flux estimates with DGVMs in Australia to decipher soil respiration processes driving the Australian terrestrial CO_2 exchange on continental scale.

Here, we investigate the decadal dataset of GOSAT CO_2 concentrations over southern hemispheric Africa from 2009 to 2018. We run a global inversion with GOSAT and in situ measurements to infer GOSAT satellite-based CO_2 exchange ~~fluxes~~ between land and atmosphere and compare the ~~fluxes~~results to ~~flux estimates~~those based on in situ measurements alone, to ~~machine learning approaches~~FLUXCOM products, and to the TRENDYv9 ensemble of DGVMs. By selecting a subset of DGVMs which match the satellite-based carbon fluxes, we ~~analyse~~analyze the underlying processes driving the IAV and seasonal variability of the southern African carbon cycle.

2 Data and Methods

2.1 Study region

65   Our study region spans southern hemispheric Africa southwards of 10° S including Madagascar (see Fig. 1). This region agrees with the region selection in Mengistu and Mengistu Tsidu (2020) taking into account the different climatic conditions in the African continent. Northwards of the study region, Africa is influenced by the low pressure system of the inter tropical convergence zone leading to a tropical wet regime. In the southern Africa, high pressure cells lead to dry conditions and cause the existence of the Kalahari Desert (Mengistu and Mengistu Tsidu, 2020). Even though total annual precipitation is

70   decreasing southwards, the whole region experiences distinct wet and dry seasons and is influenced strongly by IAV of precipitation (Fan et al., 2015; ~~Valentinti~~Valentini et al., 2015). The study region is mainly covered by (woody) savannas, grassland, and shrubland (see Fig. 1).
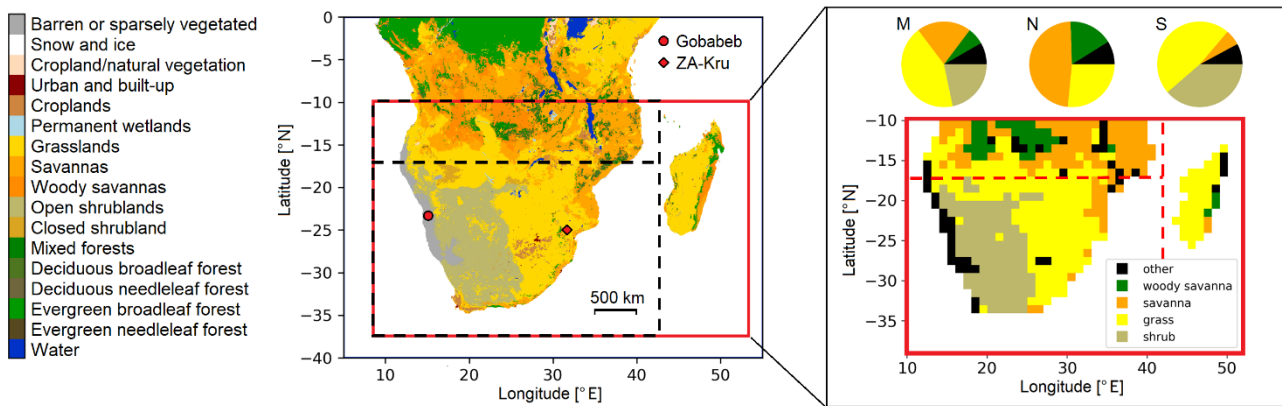
Figure 1: Study region southern Africa. The land cover in the study region is given based on MODIS (MCD12C1) data (Friedl and
75   **Sulla-Menashe, 2022). Additionally, the main region used for the analyses is depicted as a red box. ~~The black dashed boxes show~~**
~~the subdivision into a northern and southern region~~In the inlet map on the right side, the land cover is aggregated in larger land
cover classes and on a 1°x1° spatial resolution, which is used for most of the analyzed data. The main region, thereby, comprises
547 grid cells. The dashed boxes show the subdivision into a northern and southern region. Madagascar is part of the main region,
but it is excluded in the subdivision. The pie charts depict the share of the different land cover classes in the main study region
80   **(M), the northern subregion (N), and the southern subregion (S). The locations of the COCCON measurement site Gobabeb (Frey**
et al., 2021; Dubravica et al., 2021) and the flux tower in Kruger National Park (Archibald et al., 2009) are given as red circle and
diamond.

The vegetation is mostly water limited in its growth (Williams et al., 2008) and exposed to large seasonal fires. The fire season starts in May in the western part of southern hemispheric Africa and spreads eastwards to reach southern Africa in

85   September (Edwards et al., 2006). Fires on the whole African continent are the largest contributor to and account for more than half of the global fire carbon emissions (van Marle et al., 2017; Shi et al., 2015; Valentini et al., 2014). They reduce the African carbon sink significantly (Lasslop et al., 2020). We subdivide the study region in a northern, savanna dominated region and a southern grass- and shrubland region separated at 17°S, excluding Madagascar.

2.2 Total column CO_2 measurements

90 For our analyses we use column-~~average~~averaged dry-air mole fractions of CO_2 (XCO₂, in the following referred to as CO_2 concentrations) measured by the Greenhouse Gases Observing Satellite (GOSAT~~).~~) over land in our study region. GOSAT was launched in 2009 and has a sub-satellite field of view of 10.5 km radius with a sparse sampling grid. We use GOSAT CO_2 concentration data generated by applying the RemoTeC radiative transfer and retrieval algorithm version 2.4.0 (Butz, 2022) as used in Metz et al. (2023). The retrieval version covers the period 04/2009–06/2019 and is based on the preceding

95 RemoTeCv2.3.8 as used in Detmers et al. ~~(2015) and covers the period 04/2009–06/2019~~(2015). The major updates between versions 2.3.8 and 2.4.0 are stricter quality filtering in the latter and updated ancillary input data, especially for the prior gas concentrations used. Moreover, GOSAT CO_2 concentration data generated by the NASA Atmospheric CO_2 Observation from Space (ACOS) algorithm version 9 (Lite), available for the period 04/2009-~~07~~06/2020, is used~~.~~ (Taylor et al., 2022). In the following the datasets are called GOSAT/RemoTeC and GOSAT/ACOS (see Table A1 for more information about the

100 datasets and nomenclature used in this study). GOSAT/ACOS single measurements have a precision of 1.5 ppm and a mean bias of 0.2 ppm in validation against TCCON (Taylor et al., 2022). GOSAT/RemoTeC was found to have a similar precision of 1.9 ppm (Buchwitz et al., 2017) and by construction a mean bias of 0 ppm in comparison to TCCON after bias correction. GOSAT/RemoTeC was found to have a regional and seasonal systematic error of 0.6 ppm and 0.5 ppm respectively (Buchwitz et al., 2017).

105 For ~~validation~~evaluation purposes, Land-Glint and Land-Nadir (LGLN) XCO₂ data (version 11.1r) measured by the Orbiting Carbon Observatory-~~-~~2 (OCO-2) satellite is used (OCO-2/OCO-3 Science Team, ~~2020; Eldering~~2022; Jacobs et al., ~~2017~~2024). OCO-2 was launched in 2014 and has a sub-satellite field of view of 1.3 km x 2.3 km. Furthermore, Collaborative Carbon Column Observing Network (COCCON) XCO₂ data of the Gobabeb station (Namibia, Frey et al., 2021; Dubravica~~,~~ et al., 2021) is taken for comparison. COCCON stations measure XCO₂ using a sun-viewing ground-based

110 Fourier transform infrared spectrometer (Frey et al., 2019). We use the full dataset of COCCON measurements i.e. we do not apply further filtering or co-sampling to GOSAT, as there are too few coinciding GOSAT measurements.

For examining the seasonal variability of CO_2 concentrations in the study region, the global background trend is subtracted from the total CO_2 measurements to obtain detrended CO_2 concentrations. For this, we assume a yearly linear increase of global atmospheric CO_2 and use the annual mean CO_2 growth rate (GR) published by the National Oceanic and Atmospheric

115 Administration (NOAA). The growth rates are based on globally averaged CO_2 concentration measurements of marine surface sites (NOAA, 2024~~).~~) and their calculation is further described in Taylor et al. (2023, Figure A3) and Pandey et al. (2024). The following equation describes the used background trend:

$$BG_{y,m} = BG_0 + \sum_{i=2009}^{y-1}(GR_i) + \frac{m}{12}GR_y \ . \tag{1}$$

Thereby, the increase of the CO_2 concentrations in the previous years from 2009 onwards is described by the second part in

120 the equation. The increase within the previous months in the respective year is given by the third part. Both are added to an

overall offset BG_0 in 2009. This offset is estimated so that the mean of the detrended CO_2 concentrations over the whole time period is zero.

2.3 Fluxes

2.3.1 Top-down

Carbon fluxes can be obtained by assimilating measured CO_2 atmospheric concentrations in an atmospheric inversion. Atmospheric inversions typically build on Bayesian optimization i.e. they optimize forward transported CO_2 emissions such that these agree best with the observations within measurement and model uncertainties, while at the same time not deviating from the prior within given prior uncertainties. For our study, we use three in situ CO_2 measurement based atmospheric inversions: the TM5 four-dimensional variational inversion system (TM5-4DVar, ~~(Basu et al., 2013)),~~. NOAA's modelling and assimilation system CarbonTracker (CT2022, ~~(Peters et al., 2007; Jacobson et al., 2023)),~~. and Copernicus Atmosphere Monitoring Service (CAMS, ~~(Chevallier et al., 2005; Chevallier et al., 2010; Chevallier et al., 2019)).~~ The models estimate global CO_2 fluxes based on a set of in situ CO_2 measurements from global monitoring networks (Masarie et al., 2014). ~~Thereby, the~~The models use different prior datasets. For example, for the biogenic CO_2 fluxes, TM5-4DVar and CarbonTracker build on different implementations of the Carnegie-Ames-Stanford Approach (Randerson et al., 1996) as further described in Metz et al. (2023), Weir et al. (2021), and Jacobson et al. (2023), while CAMS uses biogenic fluxes of the ORCHIDEE model (Chevallier et al., 2019). Furthermore, the ~~models~~inversion systems use different transport models and inversion techniques. While TM5-4DVar and CarbonTracker use the transport model TM5, CAMS uses the LMDZ global atmospheric transport model. TM5-4DVar and CAMS make use of a four-dimensional variational data assimilation, while CarbonTracker uses an ensemble Kalman filter. All three models use ECMWF ERA5 data as meteorological drivers. The output resolution is monthly 3°x2° for TM5-4DVar and CarbonTracker2022 and monthly 3.7°×1.81° for CAMS (see Table A1 for more details). The ensemble of the three models is referred to as in-situ-only inversions in the following, TM5-4DVar based on in situ measurements is called TM5-4DVar/IS.

In addition to in situ measurements, satellite CO_2 concentration measurements can be ~~fed into~~assimilated by atmospheric inversions. To this end, we use the model TM5-4DVar and assimilate GOSAT CO_2 concentration measurements ~~together with the in situ measurements.~~over land and ocean together with the in situ measurements. We use the individual total CO_2 concentration measurements, i.e. we do not apply any detrending or spatiotemporal averaging. Detrending and spatiotemporal averaging is only applied for visualization purposes to show the variability in the monthly CO_2 concentrations (Section 3.1). Depending on the specific GOSAT dataset used, we refer to these fluxes in the following as TM5-4DVar/RemoTeC+IS, TM5-4DVar/ACOS+IS, or when using the mean of both TM5-4DVar/GOSAT+IS. More details about the TM5-4DVar settings can be found in Metz et al. (2023). For comparison we also draw on data of the OCO-2 Model Intercomparison Project (MIP) (Byrne et al., 2023) for the years 2015 to 2018. Within the MIP, atmospheric

inversions estimate carbon fluxes by assimilating OCO-2 satellite ~~CO₂ data~~XCO₂ observations together with in situ data. ~~Thereby, all~~All MIP inversion models use the same fossil fuel emission dataset but differ in the chosen datasets for all other

155 prior fluxes (Byrne et al., 2023). We specifically make use of the LNLGIS (assimilation of OCO-2 ~~satellite data~~LNLG observations together with in situ ~~data~~measurements) and the IS (assimilation of in situ ~~data~~measurements only) experiment in the following referred to as MIP/OCO-2+IS and MIP/IS, respectively. Like Byrne et al. (2023), we exclude the MIP model LoFI as it uses a non-traditional inversion scheme differing from the MIP protocol. MIP/OCO+IS and MIP/IS provide fluxes with monthly 1°x1° resolution.

160 All inversions optimize for biogenic and oceanic fluxes but impose anthropogenic fossil fuel emissions and fire emissions. The sum of (imposed) fire and biogenic fluxes yields our net biome productivity (NBP) estimates. In this study, positive fluxes denote a release of CO_2 from land into the atmosphere. All fluxes are regridded to monthly 1°x1° fluxes before performing the region selection.

By transporting the posterior fluxes after the optimization, atmospheric inversions can model posterior concentration fields,
165 which can be interpolated to the time and location of the satellite measurements for comparison. This so-called cosampling is used to eliminate sampling errors when comparing modelled concentrations to satellite measurements. We use the modelled and co-sampled posterior concentrations of the in-situ-only inversions introduced at the beginning of this section.

2.3.2 Bottom-up

We compare the top-down CO_2 fluxes to bottom-up flux datasets from DGVMs as collected by ~~the TRENDY~~
170 ~~Intercomparison v9 project.~~version 9 of the intercomparison project "trends and drivers of the regional-scale sources and sinks of carbon dioxide (TRENDY, Le Quéré et al., 2013). The project was established to support the annual global carbon budget estimation conducted by the Global Carbon Project (e.g. Friedlingstein et al., 2020). These TRENDY models give vegetation CO_2 fluxes simulated using a harmonized set of meteorological input data ~~(~~and CO_2 concentrations (Le Quéré et al., 2013; Friedlingstein et al., 2020). We use the NBP, gross primary productivity (GPP), autotrophic respiration (RA), and
175 heterotrophic respiration (RH) of 18 DGVMs (see Table A1). We thereby use the following definition:

$$NBP = NEE + fire + fluc = TER - GPP + fire + fluc = RH - NPP + fire + fluc, \qquad (2)$$

with the total ecosystem respiration (TER) calculated as sum of RA and RH, the fire emissions (fire), the land-use change fluxes (fluc), and the net primary productivity (NPP) calculated as GPP – RA. Most of the TRENDY models provide NBP fluxes directly. In the case of the models CABLE-POP and DLEM, NBP is calculated as RH-NPP, as both models do not
180 provide fire and land-use change fluxes. The spatial resolutions of the model output differ (see Table A1). Therefore, we aggregate fluxes on a monthly 1°x1° grid before applying the region selection.

Additionally, we use the FLUXCOM net ecosystem exchange (NEE) product version 1 (setup RS_V006) as described in Jung et al. (2020). FLUXCOM uses machine learning models and meteorological data to upscale eddy covariance tower CO_2 flux measurements to global scale (Tramontana et al., 2016; Jung et al., 2020). To obtain an NBP estimate, we combine the

185 NEE fluxes with fire CO_2 emissions provided by the Global Fire Emission Database (GFED, van der Werf et al., 2017). FLUXCOM and GFED are provided as 0.08°x0.08° 8-day fluxes and 0.25°x0.25° daily fluxes, respectively, and are aggregated on a monthly 1°x1° grid before applying the region selection.

2.4 Other datasets

To investigate the climatic conditions influencing the carbon fluxes, we use temperature, upper layer soil moisture, and
190 precipitation datasets of the European Centre for Medium Range Weather Forecasts (ECMWF) ERA5-land data product (Muñoz Sabater et al., 2019; Muñoz Sabater et al., 2021) with monthly resolution on a 0.25°x0.25° spatial grid. ERA5 datasets are aggregated on a 1°x1° grid before performing the region selection. Furthermore, we use Solar Induced fluorescence (SIF) measurements by the GOME-2 satellite from 2009 to 01/2018 (Joiner et al., 2023). SIF is considered proportional to GPP on monthly time scale and biome resolution (Sun et al., 2018; Joiner et al., 2018; Pierrat et al., 2022;
195 Zhang et al., 2016a; Zhang et al., 2016b). It can therefore be used as a proxy for CO_2 uptake by photosynthesis (Li et al., 2018).

3 Results

3.1 Monthly CO_2 concentrations by atmospheric inversions

200 To access the seasonal and inter-annual dynamics in southern Africa, we detrend the monthly mean CO_2 concentrations following Eq. (1) (see Data and Methods Sec. 2.2). The remaining CO_2 enhancements for the study region are shown in Fig. 2. The GOSAT measured CO_2 enhancements reveal a clear seasonal cycle with minimum concentration in the first and maximum concentrations in the second half of the year. This general seasonal timing is confirmed by the posterior concentrations of the in-situ-only inversions. However, yearly reoccurring differences between GOSAT and the in-situ-only
205 based CO_2 enhancements from September to November are clearly visible. The difference patternThereby, the spread between GOSAT/ACOS and GOSAT/RemoTeC (see also Fig. A1) is much smaller than their difference to and the spread among the in-situ-only inversions. The difference pattern between GOSAT and in-situ-only based CO_2 concentrations has already been described by Mengistu and Mengistu Tsidu (2020) and has been shown by Taylor et al. (2022). Furthermore, especially in the second half of the year, different in-situ-only inversions are not consistent as indicated by the large shading
210 in Fig. 2 Panel (a) (see also the individual models in Fig. A1A2). Reasons for these discrepancies will be further analysedanalyzed in Sect. 3.3.
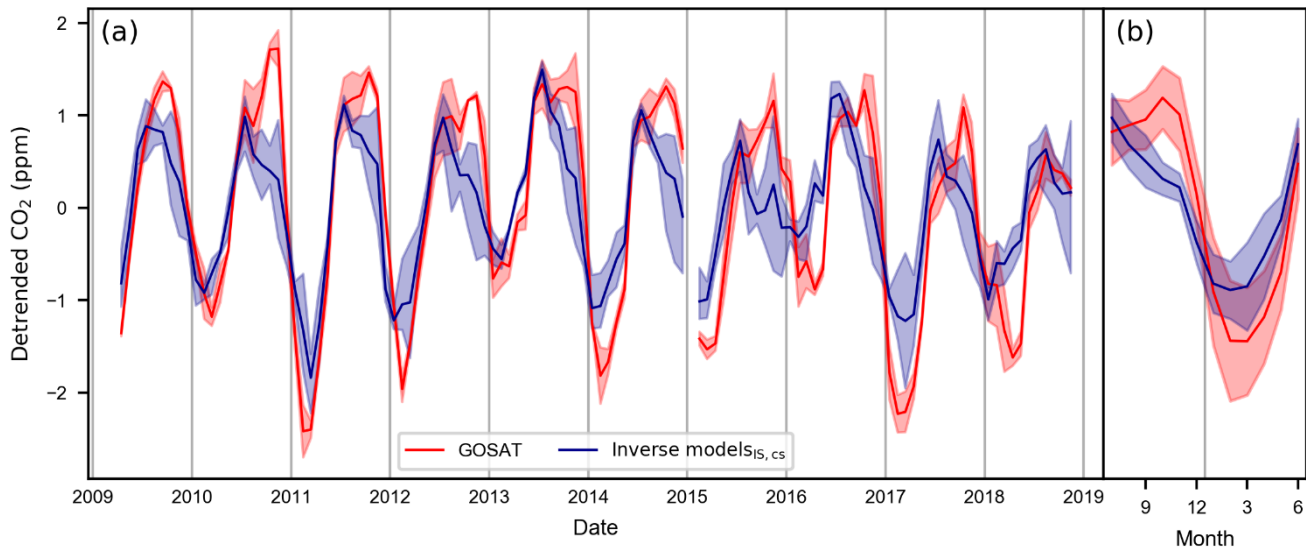
Figure 2: Monthly southern African detrended CO₂ concentrations. GOSAT measured and detrended CO₂ concentrations are depicted in red. Modelled posterior CO₂ concentrations of three in-situ-only inversions are ~~cosampled~~co-sampled (cs) on GOSAT and depicted as mean in blue. Panel (a) shows the monthly mean CO₂ concentrations. The shading indicates the range among the individual ensemble members (GOSAT/ACOS+IS and GOSAT/RemoTeC+IS in red, CT2022, CAMS, and TM5-4DVar/IS in blue). Panel (b) shows the mean seasonal cycle 2009–2018 with the standard deviation over the years as shading.

For comparison, we additionally use the OCO-2 satellite, which was launched in 2014, and one year of COCCON CO₂ column measurements in Namibia. Both datasets show a similar seasonal cycle as seen by GOSAT, i.~~.~~e. they show concentration maxima later in the year than the in-situ-only inversions (see Fig. ~~A1~~A3 and Fig. ~~A2~~A4). No other total column measurement sites (e.~~.~~g. of the COCCON network or Total Carbon Column Observing Network (TCCON, Wunch et al~~,~~.~~ (2011)) with coinciding consecutive measurements for more than one year exist in southern hemisphere continental Africa, limiting the validation possibilities of satellite total column measurements in this region.

3.2 Southern African top-down and bottom-up CO₂ fluxes
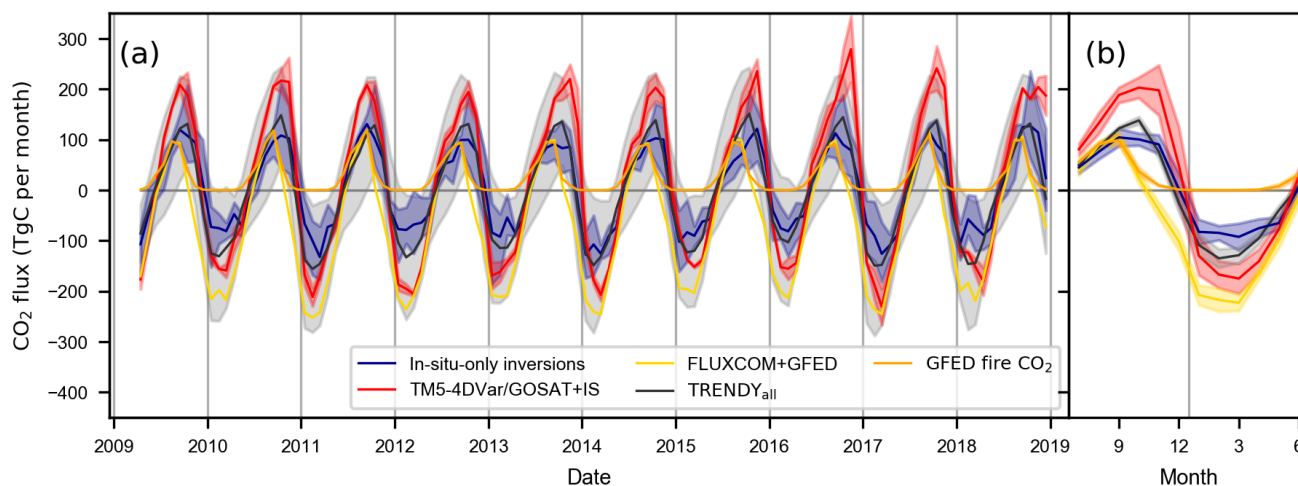
Figure 3: Top-down and bottom-up southern African net CO₂ fluxes. Panel (a) shows the mean monthly net CO₂ fluxes for the southern African region, Panel (b) shows the mean seasonal cycle of the fluxes over the 2009 to 2018 period. The TM5-4DVar/GOSAT+IS fluxes are given in red, in-situ-only inversion fluxes are shown in blue. The mean over all TRENDY models is given in grey. GFED fire emissions are shown in orange and in combination with FLUXCOM NEE in yellow. The shading indicates the range over the GOSAT based fluxes (TM5-4DVar/ACOS+IS and TM5-4DVar/RemoTeC+IS) and the in-situ-only inversion fluxes (CT2022, CAMS, and TM5-4DVar/IS) and the standard deviation over the TRENDY ensemble in Panel (a). In Panel (b) shading indicates the standard deviation over the years. Positive fluxes indicate emissions into the atmosphere. Negative fluxes correspond to an uptake of CO₂ into the land surface.

Assimilating the GOSAT CO₂ concentration measurements in TM5-4DVar, we obtain GOSAT based top-down fluxes in monthly resolution for the study region (see ~~methods~~ Sec. 2.3.1). As for the concentrations, a clear seasonal cycle is visible (Fig. 3). From January to May CO₂ is taken up by the land surface with a maximum uptake around March. From June to December, CO₂ is released into the atmosphere and reaches a maximum flux in September to November. The number of GOSAT measurements (see Fig. A5 and Fig. A6) is variable throughout the year with the smallest numbers occurring during the rainy season around December and January. This leads to larger uncertainties in the monthly mean satellite CO₂ concentrations and satellite-based fluxes during the transition from maximum to minimum concentrations and fluxes.

A similar timing of the seasonal cycle is also captured by the in-situ-only inversion fluxes (CAMS, CT2022, and TM5-4DVar/IS). However, the in-situ-only inversions' seasonal amplitude is smaller than for TM5-4DVar/GOSAT+IS.

To ~~analyse~~ analyze the found differences between TM5-4DVar/GOSAT+IS and the in-situ-only atmospheric inversions, we evaluate the information content provided by the measurements about the southern African carbon fluxes. To this end, we compare the TM5-4DVar fluxes (TM5-4DVar/IS and TM5-4DVar/GOSAT+IS) to the prior fluxes of the inversion model. From Fig. 4 it becomes clear that the in-situ-only fluxes (TM5-4DVar/IS) mainly follow the dynamics of the prior fluxes, whereas the GOSAT based fluxes deviate significantly from the prior. This is expected as the sparse coverage of in situ measurements in Africa and the southern hemisphere in general provides only little information about the African carbon

fluxes. In contrast, satellites provide nearly global coverage of CO₂ measurements. Using these measurements in TM5-4DVar, new information about the southern African carbon fluxes can be obtained and lead to a deviation of TM5-4DVar/GOSAT+IS from the prior. This finding also explains the differences among the three in-situ-only inversions (see

255   shaded range of the in-situ-only inversions in Fig. 3). The inversions assume different prior fluxes, which they follow closely, as the information of the in situ data does not substantially inform the inversion.
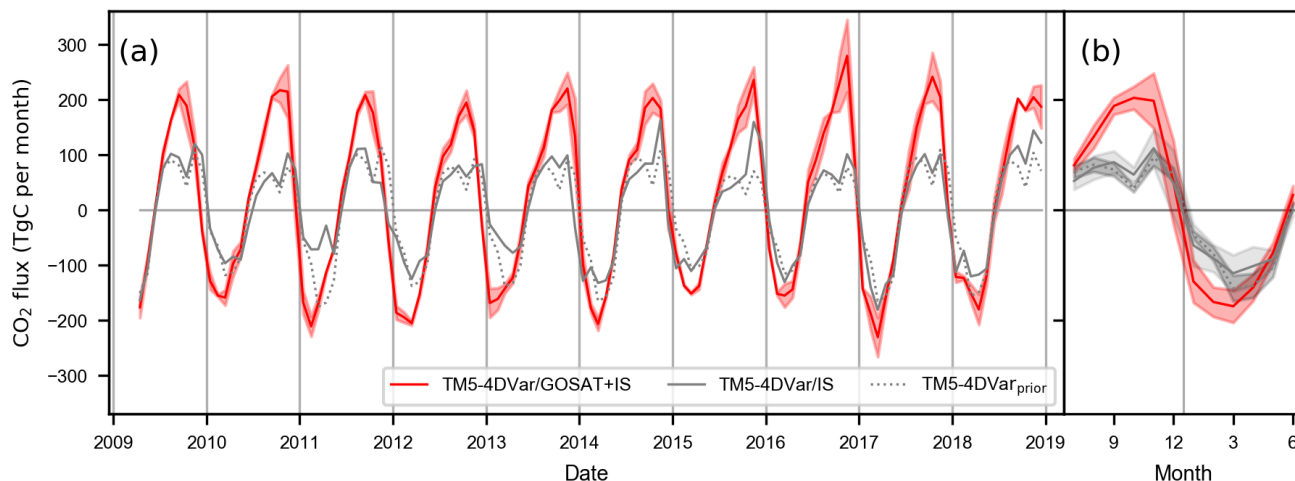
Figure 4: Top-down southern African net CO₂ fluxes from TM5-4DVar. In Panel (a), mean monthly net CO₂ fluxes for the southern African region from the TM5-4DVar prior (grey dotted), the in-situ-only inversion TM5-4DVar/IS (grey solid) and the
260   **TM5-4DVar/GOSAT+IS inversion (red) are given. Red shading indicates the range of the TM5-4DVar/ACOS+IS and TM5-4DVar/RemoTeC+IS inversions. Panel (b) shows the mean seasonal cycle 2009–2018 with the standard deviation over the years as shading.**

When assimilating OCO-2 satellite measurements instead of GOSAT measurements, the MIP/OCO-2+IS ensemble mean also shows a larger amplitude of the southern African carbon fluxes compared to in-situ-only inversions and MIP/IS (Fig. 5).

265   However, the spread among the MIP/OCO-2+IS models is large, especially during the maximum emissions from September to November. Some models show lower emissions similar to the in-situ-only inversions, whereas others agree with TM5-4DVar/GOSAT+IS. By ~~analysing~~analyzing the performance of the individual models in these three months, we find that three MIP/OCO-2+IS models reproduce the OCO-2 measurements the best (see Fig. ~~A3~~A7) indicating that the OCO-2 measurements were given a considerable weight in the inversion and thus, that the optimized fluxes were informed by

270   measurements (see Text A1). At the same time, these three inversion models (Baker, CAMS, and TM5-4DVar/OCO-2+IS) show the largest CO₂ emissions and agree best with TM5-4DVar/GOSAT+IS (see Fig.5 and Fig. ~~A3).~~ A7-A9). Still, their estimated emissions are slightly lower than those of TM5-4DVar/GOSAT+IS. When directly comparing the two TM5-4DVar inversions TM5-4DVar/GOSAT+IS and TM5-4DVar/OCO-2+IS (Fig. 5), the latter has smaller emissions. This is most likely a result of the slightly smaller seasonal amplitude of the CO₂ concentrations measured by OCO-2 compared to

275   GOSAT (see Fig. A3).

Concluding, we find that satellite-based inversions, which are actually compatible to the satellite measurements, show larger carbon fluxes in southern Africa than in-situ-only inversions, which suffer from the limited information provided by the sparse in situ measurements for southern Africa. Our results support current studies (e.g. Basu et al., 2013; Sellers et al., 2018; He et al., 2023) reporting that satellite observations do well inform atmospheric inversions for flux estimates on sub-continental scales. Satellite CO_2 concentration measurements, therefore, provide a unique information source and are especially valuable in regions with sparse in situ measurement coverage. The already long record provided by GOSAT will be more and more complemented over time by the growing record of OCO-2 and future CO_2 sensors providing even more extensive measurements.
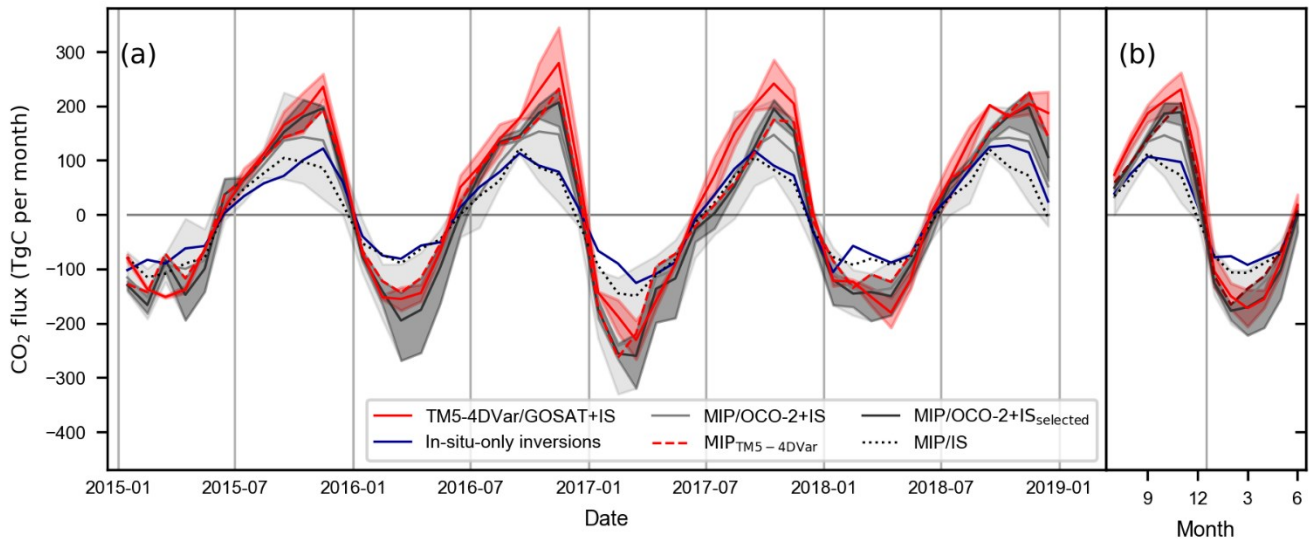
Figure 5: Top-down southern African net CO₂ fluxes from MIP. In Panel (a) mean monthly net CO₂ fluxes for the study region are given by TM5-4DVar/GOSAT+IS in red, the MIP/OCO-2+IS ensemble mean in grey, ~~and~~ the mean over three selected MIP models (CAMS, TM5-4DVar, and Baker) in black, and TM5-4DVar/OCO-2+IS as part of the MIP ensemble in red dashed. In-situ-only inversion fluxes are given in blue as mean of CAMS, CT2022 and TM5-4Dvar/IS and in black dotted from the MIP/IS ensemble. The shading indicates the range over the GOSAT fluxes (TM5-4DVar/ACOS+IS and TM5-4DVar/RemoTeC+IS), the MIP ensemble, and the three selected MIP models. Panel (b) gives the mean seasonal cycle from 2015 to 2018 with shading indicating the range over the MIP ensembles' models and the standard deviation of the TM5-4DVar/GOSAT+IS over the years.

Next to the in-situ-only inversion fluxes, we compare the TM5-4DVar/GOSAT+IS fluxes to FLUXCOM CO₂ fluxes. As FLUXCOM only provides NEE fluxes, we add GFED fire CO₂ emissions to obtain ~~a~~an NBP estimate. In Fig. 3, FLUXCOM+GFED only reaches positive monthly fluxes from June to September due to fire emissions occurring during that time. From October to May it shows a net CO₂ uptake. While the timing of the maximum sink agrees well between FLUXCOM+GFED and the inversion fluxes, FLUXCOM+GFED shows a smaller amplitude and an earlier drop in emissions compared to TM5-4DVar/GOSAT+IS and in-situ-only inversion fluxes. The tendency of FLUXCOM to report a stronger carbon sink on the southern hemisphere compared to other datasets is described in Jung et al. (2020). It is expected

that the sparsity of eddy-covariance towers in Africa or in similar ecosystems hampers the machine-learning based approach

300   of FLUXCOM for estimating CO_2 fluxes in the study area. Jung et al. (2020) describe larger uncertainties due to representation errors in semi-arid regions.

Finally, we compare the inversion results to the ensemble of ~~processed~~ process-based vegetation models of the TRENDYv9 project. The mean of the DGVM ensemble in Panel (a) of Fig. 3 shows a smaller amplitude than the GOSAT fluxes and compares with the in-situ-only inversion fluxes. However, as indicated by the large standard deviation, the models deviate

305   substantially from each other. Foster et al. (2024) and Metz et al. (2023) observed a similar large spread among DGVMs for the North American Temperate region and Australia, respectively. Both studies highlight the importance of performing a sub-selection of DGVMs agreeing well with atmospheric CO_2 measurements.

3.3 GOSAT and SIF atmospheric constraints on TRENDY models

Given the large spread of the TRENDY models, we select DGVMs according to their agreement with the GOSAT based

310   CO_2 fluxes and SIF. Thereby, in a first step, we compare the monthly mean DGVM and TM5-4DVar/GOSAT+IS NBP and NEE fluxes based on the RMSE of the monthly fluxes and the agreement in the seasonality. ~~For~~In a second step, only for the well matching DGVMs, we additionally compare the GPP normalized mean seasonal cycle to the GOME SIF normalized mean seasonal cycle. Only models with a timing of the minimum and maximum GPP agreeing within +-1 month with the normalized SIF seasonal cycle are selected (see Fig. 6). This ensures the correct seasonal timing of the modelled GPP fluxes.

315   Based on these criteria, we select the models ORCHIDEE (RMSE NBP: 60.2 TgC/month, RMSE NEE: 68,2 TgC/month), ORCHIDEEv3 (RMSE NBP 70.2 TgC/month, RMSE NEE: 56.2 TgC/month) and CABLE-POP (RMSE NBP: 78.2 TgC/month, RMSE NEE: 63.6 TgC/month). ~~The~~ All other models, except for the model OCN, ~~which~~already were excluded in the first step of NBP/NEE comparison. OCN performs well ~~for~~in the NBP/NEE~~,~~ comparison but shows larger deviations in the SIF/GPP comparison (see Fig. ~~6)~~6). Therefore, it was excluded in the second selection step and is ~~therefore~~ not

320   included in the TRENDY selection. The exclusion of OCN underlines the importance of the SIF/GPP selection and demonstrates that a correct timing of the net CO_2 exchange fluxes does not necessarily imply the correctness of the modelled gross fluxes. In general, it is noteworthy that only three out of 18 TRENDY models pass our selection process. This again reveals the large uncertainties associated with the TRENDY ensemble estimate for semi-arid southern hemispheric Africa.

325
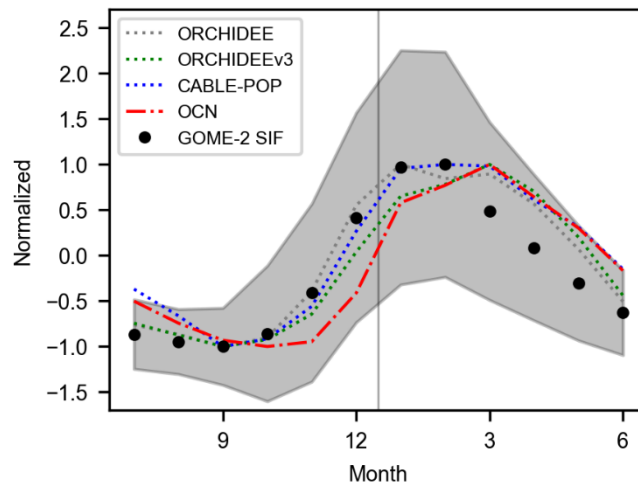
Figure 6: Seasonal cycle of SIF and selected TRENDY models. The normalized mean seasonal cycle of GOME-2 SIF (2009–01/2018), the three selected DGVMs (ORCHIDEE, ORCHIDEEv3, CABLE-POP) GPP, and OCN GPP (2009–2018) are shown in solid black ~~and coloured~~, colored dotted, and red dashdotted, respectively. The spatial standard deviation over monthly GOME-2 SIF aggregated on a 1°x1° is given as shading.

330   The NBP mean over these three models is given in Panels (a) and (b) of Fig. 7. The models reproduce the timing and strength of the TM5-4DVar/GOSAT+IS NBP fluxes. Only at the beginning of the emission period around July to September, the TRENDY selection fluxes are lower. Furthermore, the selection shows a significantly smaller sink in 2012 and smaller source in 2016. Note that ORCHIDEE is part of the TRENDY selection and is also used by the in-situ-only inversion CAMS as prior flux assumption. This explains why CAMS best matches TM5-4DVar/GOSAT+IS CO_2 fluxes and GOSAT CO_2

335   concentrations ~~in~~(see Fig. ~~3~~A2 and Fig. ~~2~~A7, respectively~~.~~).

Fire emissions contribute substantially to the seasonality of the southern African carbon fluxes. They largely explain the beginning of the emission period from July to September (see Fig. 3). Different fire emission data products differ significantly and suggest large uncertainties on the magnitude of the actual fire emissions in our study region (see Fig. ~~A4~~A10). GFED, which we use for our analyses, shows the largest fire emissions but could even underestimate the actual

340   emissions as suggested by current literature for southern hemispheric Africa (Ramo et al., 2021, van der Velde et al., 2024).

To exclude the influence of fire emission in the comparison, we ~~analyse~~analyze the monthly NEE fluxes of the TRENDY selection compared to the TM5-4DVar/GOSAT+IS NBP fluxes with GFED fire emissions subtracted. The subtraction of the fire emissions leads to a better agreement between both datasets, especially at the beginning of the emission period suggesting that fire fluxes in the DGVMs do not agree to the GFED fire fluxes (see Fig. 7 Panels (c) and (d)). This goes

345   along with large uncertainties in DGVM fire fluxes being reported previously (Bastos et al., 2020).
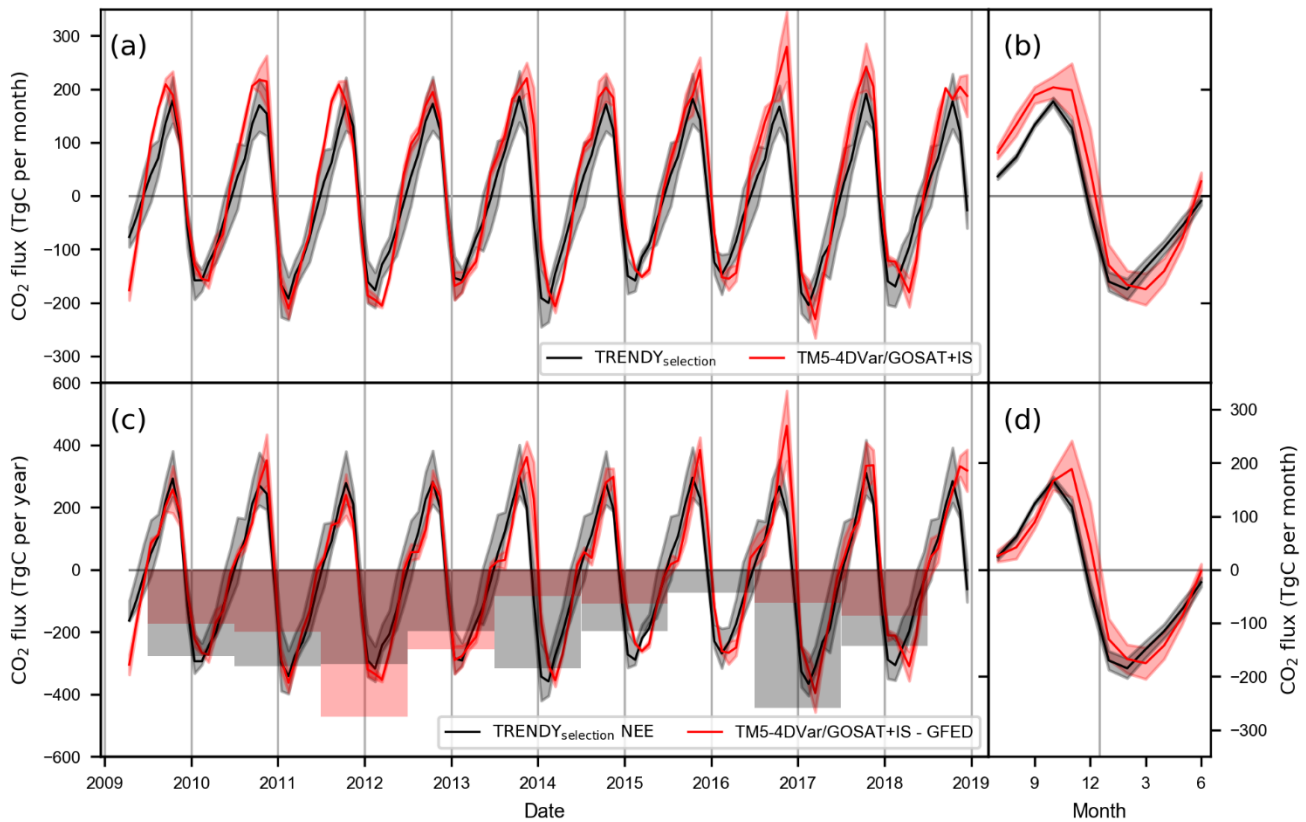
Figure 7: Annual and mean monthly NBP and NEE fluxes in southern Africa. The NBP fluxes by TM5-4DVar/GOSAT+IS (red) and selected TRENDY models (black) are given as mean monthly fluxes in Panel (a) and as the mean seasonal cycle in Panel (b). Similar to that, Panel (c) and (d) show the monthly NEE fluxes (GFED is subtracted from TM5-4DVar/GOSAT+IS). Additionally, the annual (July to June) NEE fluxes of the selected TRENDY models and TM5-4DVar/GOSAT+IS – GFED fluxes are given. The shading indicates the standard deviation over the TRENDY models and range of TM5-4DVar/ACOS+IS and TM5-4DVar/RemoTeC+IS (Panel (a) and (c)) and over the years (Panel (b) and (d)).

Panel (c) in Fig. 7 additionally shows the annual NEE fluxes (July-June) as bars. The absolute difference between TM5-4DVar/GOSAT+IS and TRENDY annual fluxes is large in some years. These differences are caused by a stronger sink at the beginning of 2012 and enhanced emissions at the end of 2013 and 2016 in TM5-4DVar/GOSAT+IS compared to TRENDY. However, while both datasets do not agree on the absolute value of annual fluxes in most of the years, they show a similar IAV. Both datasets show a slightly stronger CO_2 uptake from 2010 to 2012. These years were strong and moderate La ~~Nina~~Niña years with enhanced rainfall in 2010 and 2011 in the study region compared to the longtime mean (see Fig. ~~A5~~A11). Additionally, lower than average temperatures led to enhanced ~~surface near~~ soil moisture near the surface in 2010/11. The soil moisture declined in 2012 to reach the long-term average. In 2015 and 2016, the sink given by the GOSAT and TRENDY selection NEE fluxes is small. These two years have been a weak and a strong El ~~Nino~~Niño year respectively with dry conditions and in case of 2016 exceptionally high temperatures (see Fig. ~~A5~~A11). These findings agree well with

results from Pan et al. (2020) pointing out that temperature and precipitation extremes impact the African ecosystems heavily and therefore play a key role in the African carbon fluxes.

365 To conclude, especially the monthly NEE and NBP fluxes, but also the IAV of the selected TRENDY models agree well with TM5-4DVar/GOSAT+IS NEE and NBP – although the latter was not a criterion in the selection process of the TRENDY models. This suggests that the selected models indeed capture the carbon cycle dynamics even on a decadal time scale. For this reason, we use the model selection for further investigations of vegetation processes driving the southern African carbon cycle.
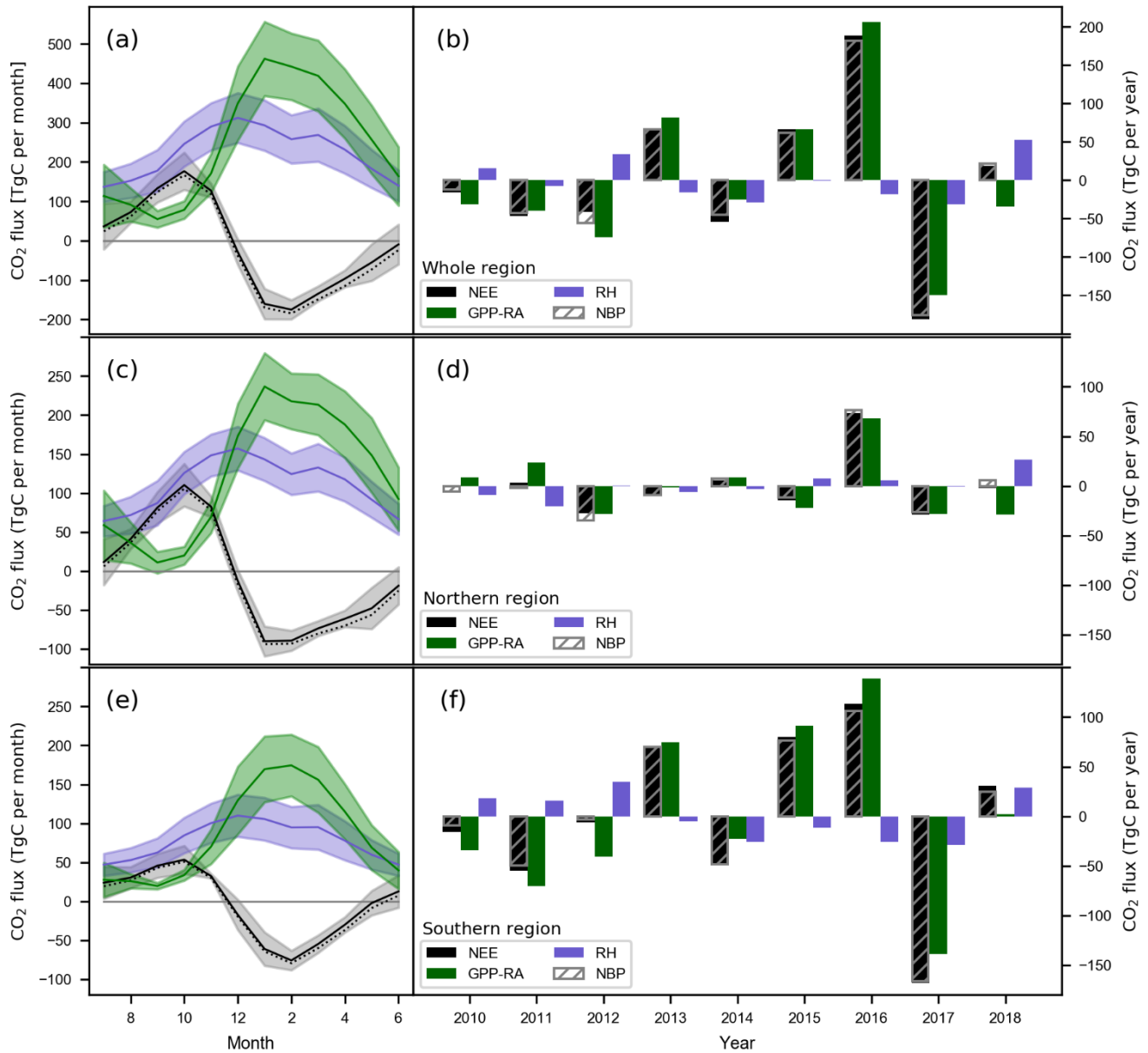
Figure 8: Annual and mean monthly CO₂ net and gross fluxes. The mean monthly fluxes (Panel (a), (c), (e)) and annual **(July to June)** anomalies (Panel (b), (d), (f)) of NBP, NEE, GPP-RA, and RH of the selected TRENDY models are given in black, grey (dotted), green, and blue, respectively. The fluxes are given for the whole study region (Panel (a) and (b)), the Savanna dominated northern region (north of 17°S, Panel (c) and (d)), and the southern region with grass- and shrubland (Panel (e) and (f)). The annual anomalies are calculated by subtracting the individual long-term mean of the annual fluxes. Thereby, a positive GPP anomaly denotes a reduced GPP and vice versa. The shading in Panel (a), (c), and (e) indicates the standard deviation over the three selected models (ORCHIDEE, ORCHIDEEv3, and CABLE-POP).

To investigate the vegetation dynamics shaping the seasonal cycle of the southern African CO_2 exchange ~~fluxes~~, we use the selected TRENDY models to further split up the net ecosystem exchange fluxes ~~in~~into the gross fluxes NPP (GPP – RA) and RH. The gross and net fluxes are given as mean seasonal cycle and annual anomalies in Fig. 8. In the mean seasonal cycle for the whole study region (Panel (a)), we can see a clear difference in timing between RH and GPP-RA. ~~RH~~Heterotrophic respiration increases early in September and October, while RA increases one to two months later simultaneously with GPP (see Fig. ~~A6~~A12). The dephasing between RH and GPP-RA leads to a prolonged emission phase in the net CO_2 exchange. It takes place in the whole region and occurs in the savanna dominated north (Fig. 8 Panel (c)) and in the grass- and shrublands in the south (Panel (e)). The dephasing takes place in every year (see Fig. ~~A7~~A13) and is present in all selected TRENDY models. It causes a mean CO_2 release of 494 TgC during the emission phase, which is about 17% and 18% of the annual total RH and GPP-RA, respectively.

When looking at the monthly precipitation over the study region (see Fig. ~~A8~~A14) one can identify a distinct drought phase occurring in the whole study region. The subsequent start of the rainy season in September and October temporally coincides with the early increase in RH. This finding resembles the results of Metz et al. (2023) in Australia, describing an increase of soil respiration with the beginning of the rainy season prior to the start of the growing season. The study finds soil respiration pulses resulting from rewetting of soils to cause the continental scale increase of soil respiration. Such soil respiration pulses at local arid sites are discussed in the context of the Birch effect (Birch et al., 1964; Jarvis et al., 2007). Thereby the rewetting of the soil enables microbial populations to grow and to transform the carbon stored in the soils into CO_2 emissions. CO_2 is then released in substantial amounts within a short period of time. Like in Metz et al. (2023), we find short duration emission pulses in the daily flux record of a FLUXNET station in the study region. Exemplary annual records of the FLUXNET station in the Kruger National Park (Archibald et al., 2009) show CO_2 emission caused by precipitation pulses (see Fig. ~~A9~~A15). This is also reported in Fan et al. (2015) studying a two-year measurement record of carbon fluxes in Kruger National Park in more detail. The study finds recurring respiration emission pulses due to precipitation events and attributes them to the Birch effect. The TM5-4DVar/GOSAT+IS fluxes indicate an even larger time lag between the increase of soil respiration and NPP in some years compared to TRENDY. ~~A by 1-2 months~~A prolonged emission phase of an additional 1 to 2 months (see Figure 7, Panel (c)) takes place in years with especially low soil moisture (2013, 2015, 2016, see Fig. ~~A5~~A11). This later drop in emissions could either be caused by a delayed start of the GPP rise in the growing season or enhanced soil respiration due to the drier conditions~~.~~ causing an enhanced accumulation of soil carbon during the years. It is not possible to investigate this further, as none of the TRENDY DGVMs captured the IAV in the timing of the emission phase.

It is noteworthy that large parts of the not selected 'other' TRENDY models miss the dephasing between RH and GPP-RA. Their NBP estimates, therefore, do not agree with the emissions around October found by the satellite inversion. Implementing soil respiration due to rewetting more accurately in those models could improve their agreement with the satellite-based fluxes. Metz et al. (2023) found that the dephasing in the TRENDY models is most likely caused by a different response time of soil respiration and vegetation growth on precipitation e.g. water needs to percolate into the deeper

soil layers with plant roots to initiate plant growth, whereas heterotrophic respiration is driven by upper soil layer soil moisture or precipitation. The implementation of such a time lag between heterotrophic respiration and GPP seems to be a necessary but not sufficient prerequisite to accurately capture the seasonal carbon flux variability in semi-arid southern Africa. Our results call for studies on how to implement the response of ecosystems on soil rewetting more accurately to improve the consistency and accuracy of the TRENDY ensemble in semi-arid regions.

Looking at the annual gross flux anomalies given by the TRENDY selection (Fig. 8, Panel (b)), we see that the IAV of NBP and NEE is driven by GPP mainly. Enhanced GPP from 2010 to 2012 leads to a constant stronger uptake of CO_2. In 2017 a strongly enhanced GPP causes a large CO_2 sink. Reduced GPP in 2013, 2015, and 2016 results in positive NEE anomalies associated with a reduced sink in NEE. RH only plays a minor role and mostly slightly counteracts the GPP anomalies. These findings agree with the studies of Ciais et al. (2009), Weber et al. (2009), and Williams et al. (2008) which identify GPP variability as a major source of African fluxes' IAV. ~~This is~~ It is, however, in contrast to semi-arid Australia, where Metz et al. (2023) found large IAV of RH driven by precipitation anomalies during the dry season. The African study region, however, has a distinct and regular dry season every year (see Fig. ~~A8~~A14), leading to a smaller influence of RH on IAV. Note that in 2017, GOSAT suggests a much smaller annual CO_2 sink. However, the discrepancy is mainly caused by a significant difference in the emissions in the second half of the year and while both datasets agree well in the phase of carbon uptake (see Fig. 7, Panel (c)). Therefore, the TM5-4DVar/GOSAT+IS fluxes support the large GPP anomaly given by the TRENDY models but suggest stronger respiration or fire fluxes at the end of 2016. ~~Looking at the subregions (Panels (d) and (f)), one can see that the sinks in 2010-2012 and 2017 are mainly driven by the southern grassland region, whereas the comparably large release in 2016 seems to be driven by the whole African region.~~ ~~These findings agree with the studies of Ciais et al. (2009), Weber et al. (2009), and Williams et al. (2008) which identify GPP variability as a major source of African fluxes' IAV.~~

Looking at the subregions (Panels (d) and (f)), one can see that the sinks in 2010, 2011 and 2017 are mainly driven by the southern grassland region, where enhanced precipitation occurred during these years (see Fig. A11). The comparably large release in 2016 seems to be driven by the whole African region experiencing the highest annual temperatures and driest conditions within the 10-year study period. Therefore, GPP IAV seems to be heavily impacted by precipitation variability. According to GFED (see Fig. A10), fire emissions play a minor role in impacting GPP and driving NBP anomalies. The variability of fire emissions is much lower than for NBP and GPP-RA. In the whole study region, IAV (calculated as standard deviation over the years) of GPP-RA and NBP fluxes are 97.7 TgC/year and 94.1 TgC/year, respectively. IAV of GFED fire emissions is 27.3 TgC/year, similarly low as IAV of RH (27.1 TgC/year). Furthermore, the annual fire emissions do not amplify the trend of the NBP anomalies. They have been on a normal level during the large positive NBP anomaly in 2016. Higher than average fire emissions counteract the sink anomalies in 2011 – 2012 and only the slightly reduced fires in 2017 amplify the sink anomaly.

4 Conclusions

The sparsity of in situ CO_2 concentration and flux measurements cause large uncertainties in carbon flux estimates in the southern African region. We show that satellite measurements provide additional information leading to an improvement of our knowledge about the southern African carbon cycle. Our study demonstrates that satellite measurement based atmospheric inversions and SIF can be used as atmospheric constraints for sub-selecting TRENDY DGVMs. This is necessary as TRENDY flux estimates show a large spread in our study region.

Using the satellite based selection of TRENDY DGVMs, we find that IAV of NBP and NEE in southern Africa is driven by GPP variability. ~~Thereby,~~ This supports findings by Ciais et al. (2009), Weber et al. (2009), and Williams et al. (2008) using individual vegetation models. The enhancements in annual GPP mainly originate in the grass- and shrublands in the southern part of the study region. and occur in years with enhanced amount of precipitation. The seasonal variability of the southern African carbon fluxes is impacted by soil respiration dynamics, which are driven by the onset of the rainy season. Respiration pulses have been reported under the term of the Birch effect for arid Africa (Fan et al., 2015) and have been shown to be relevant on continental scale in semi-arid Australia (Metz et al., 2023). This enforces the relevance of rain ~~induces~~ induced CO_2 emissions for the southern African region and semi-arid regions in general. Our results emphasize the importance of correctly representing the response of semi-arid ecosystems to soil rewetting in DGVMs (e.g. different response times of RH and GPP), as this was found to be a prerequisite to accurately capture the seasonal carbon cycle dynamics.

Appendix A

Figure A1Text A1: The performance of the individual MIP models.

In Fig. 5, the ensemble mean of MIP/OCO-2+IS shows lower emissions than TM5-4DVar/GOSAT+IS in the second half of the year. A selection of three models (Baker, TM5-4DVar, and CAMS), however, shows larger fluxes and agrees better with the GOSAT based fluxes (see Section 3.2 and Fig. 5). Next to the OCO-2 informed posterior fluxes used for the analysis in the main text, the MIP/OCO-2+IS dataset provides the prior fluxes used by the individual MIP models. Furthermore, 5% of the OCO-2 measurements are withheld for validation purposes and modelled XCO_2 co-sampled on the left-out measurements are provided for each model but CSU. The OCO-2 co-samples and the prior fluxes of the MIP models can be used to further evaluate the differences between the three selected models and the other MIP models.

In Fig. A7, the mismatch between XCO_2 modelled by MIP and XCO_2 measured by OCO-2 is given for the months of the strongest emissions (September to November). The XCO_2 mismatch is the smallest for the three selected models, Baker, TM5-4DVar, and CAMS, which have at the same time the smallest mismatch to TM5-4DVar/GOSAT+IS. Hence, the models which reproduce the OCO-2 measurements best, also agree best with the GOSAT based CO_2 fluxes.

The difference between posterior and prior fluxes for the MIP models are given in Fig. A8. TM5-4DVar and Baker have the largest differences between the posterior and prior fluxes. Therefore, it is likely that even though the prior fluxes of TM5-4DVar and Baker deviate strongly from the GOSAT based fluxes (see Fig, A9), considerable weight was given to the OCO-2 measurements in the inversion. As a result, the posterior fluxes are closer to the GOSAT based fluxes than to their prior fluxes (Fig. A8). As the CAMS prior already agrees reasonably well with TM5-4DVar/GOSAT+IS fluxes, no conclusion on the weights can be drawn here.

The other MIP models, which have lower emission fluxes, show larger mismatches to the OCO-2 XCO_2 measurements for September to November (Fig. A7). Although, for most of these models, assimilating OCO-2 increases the emission fluxes and reduces the difference to the GOSAT based fluxes (see Fig. A8 and Fig. A9), the changes (i.e. the difference between posterior and prior fluxes) are small compared to TM5-4DVar and Baker (see Fig. A8). The larger mismatch to OCO-2 XCO_2 and the smaller posterior – prior flux differences seem to indicate that a smaller weight was given to the OCO-2 measurements compared to the selected MIP models.

In general, the GOSAT flux mismatch and the OCO-2 XCO_2 mismatch is larger in October and November than in September. This is most likely caused by the prior fluxes in September already being closer to the GOSAT based fluxes than in the other two months (see panel b in Figure A9).
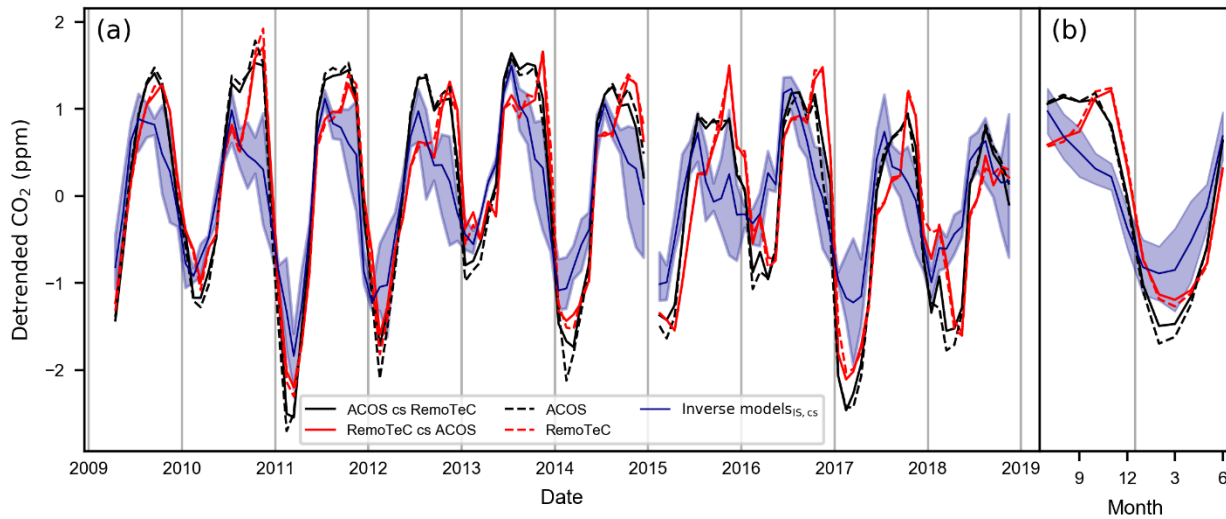
Figure A1: Monthly southern African detrended CO_2 concentrations measured by GOSAT. GOSAT/ACOS is given in black, GOSAT/RemoTeC is given in red. Dashed lines show the mean CO_2 concentrations over the whole dataset. The mean CO_2 concentrations of the soundings included in both datasets, ACOS and RemoTeC, are given as solid line. CS stands for co-sampled and indicates that only soundings, also included in the other dataset are considered. The deviations due to different sampling are in sub-ppm scale and do not explain the differences between ACOS and RemoTeC. Modelled posterior CO_2 concentrations of the in-situ-only inversions are co-sampled (cs) on GOSAT and depicted as mean in blue for comparison. The shading indicates the range among the individual in-situ-only inversions. Panel (b) shows the mean seasonal cycle 2009–2018 with the standard deviation over the years as shading.
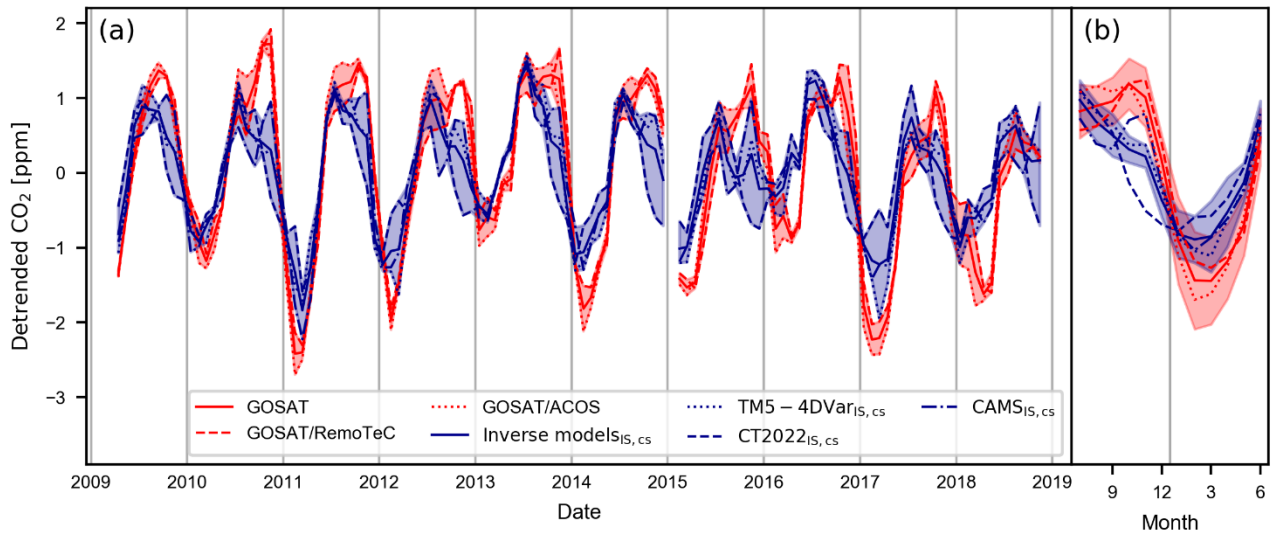
Figure A2: Monthly southern African detrended CO₂ concentrations given by inversions and satellites. Like Fig. 1, but with detrended XCO₂ ~~measurements of OCO-2 in black und~~of individual in-situ-only inversions co-sampled (cs) on the GOSAT measurements in dark blue (CT2022 dashed, CAMS dash-dotted, and TM5-4DVar/IS dotted). Panel (a) gives the monthly mean CO₂ concentrations, while Panel (b) shows the mean seasonal cycle ~~2015~~2009-2018. The shading indicates the range among GOSAT/ACOS and GOSAT/RemoTeC and the range among the three in-situ-only inversions in Panel (a). In Panel (b) the shading indicates the standard deviation over the year.
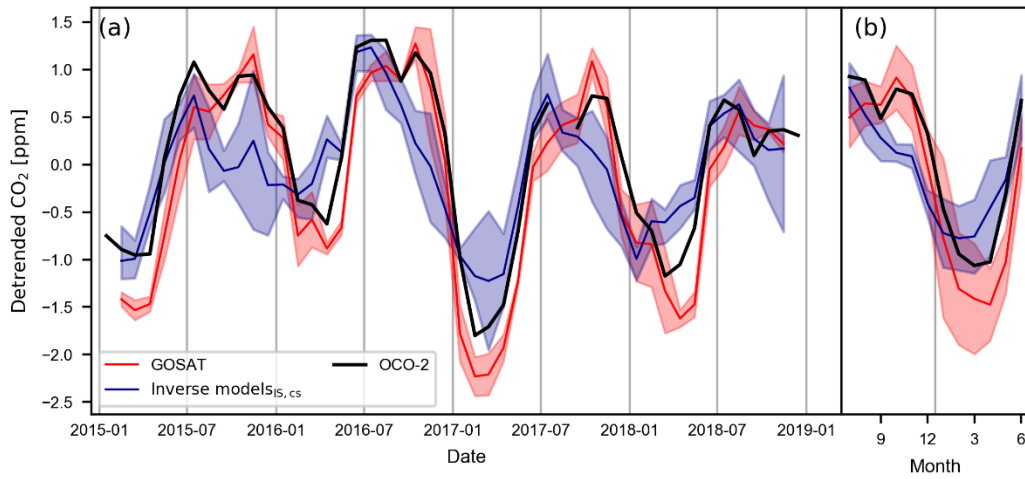
515 **Figure A3: Monthly southern African detrended CO₂ concentrations given by inversions and satellites. Like Fig. 1, but with detrended XCO₂ measurements of OCO-2 in black for the time period from 2015 to 2018. Panel (a) gives the monthly mean CO₂ concentrations, while Panel (b) shows the mean seasonal cycle 2015-2018. The shading indicates the range among GOSAT/ACOS and GOSAT/RemoTeC and the range among the three in-situ-only inversions in Panel (a). In Panel (b) the shading indicates the standard deviation over the years.**

520
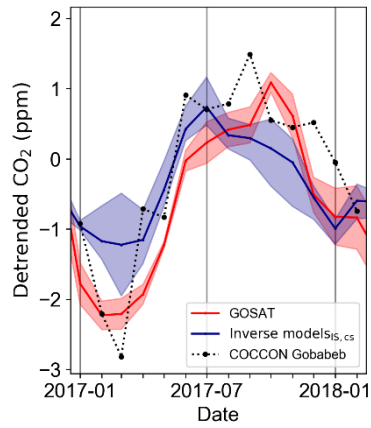
Figure A4: Monthly southern African detrended CO₂ concentrations given by inversions, satellites and COCCON measurements. Like Fig. 1, but only for 01/2017-02/2018 and with detrended XCO₂ measurements of the COCCON stations Gobabeb in black. The full dataset of COCCON measurements is used, without performing a co-sampling on GOSAT measurements nor further filtering.

~~Figure A3: Performance of the individual MIP models.~~
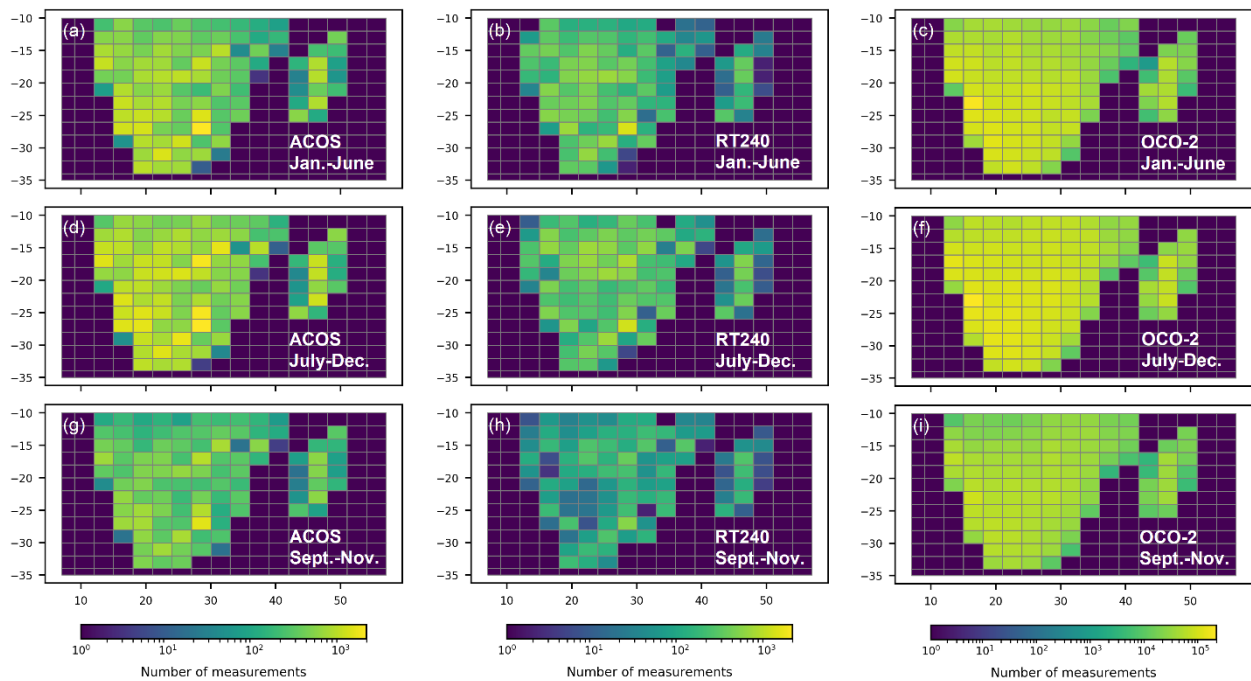
530 **Figure A5: Number and distribution of satellite CO_2 concentration measurements above southern Africa. (a), (d), and (g) Total number of GOSAT/ACOS, (b), (e), and (h) GOSAT/RemoTeC, and (c), (f), and (i) OCO-2 data per 3°x2° grid cell for (a) - (c) the months of carbon uptake (January – June), (d) - (f) the emission season (July – December), and (g) – (i) the month with the strongest emissions. GOSAT/ACOS and GOSAT/RemoTeC measurements from 2009 to 2018 and OCO-2 measurements from 09/2014 to 2018 are included. The maximum of the color scale is the same for all time periods, but different for OCO-2 than for**
535 **GOSAT/ACOS and GOSAT/RemoTeC. Compared to GOSAT/ACOS, GOSAT/RemoTeC has a reduced number of measurements, as RemoTeC algorithm applies stricter filtering of the GOSAT soundings.**
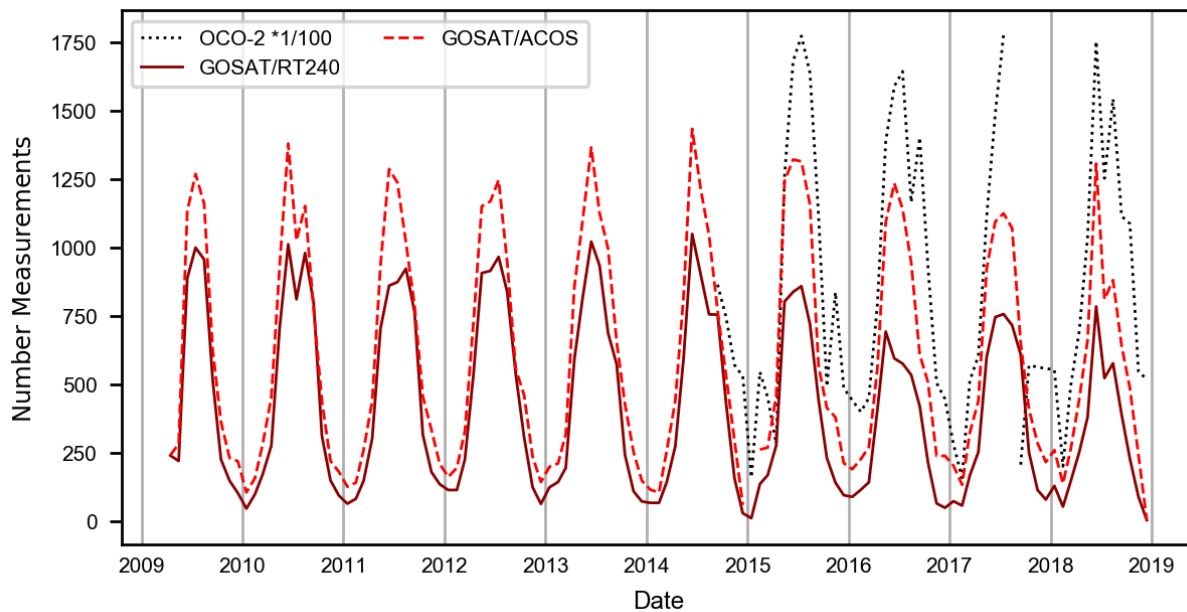
540

Figure A6: Number of satellite measurements per month. The amount of satellite measurements of the GOSAT/ACOS (red dashed), GOSAT/RemoTeC (dark red solid), and OCO-2 (grey dotted) dataset are given. Note that the number of OCO-2 measurements is shown divided by 100 to enable a comparison to the much less abundant GOSAT measurements.
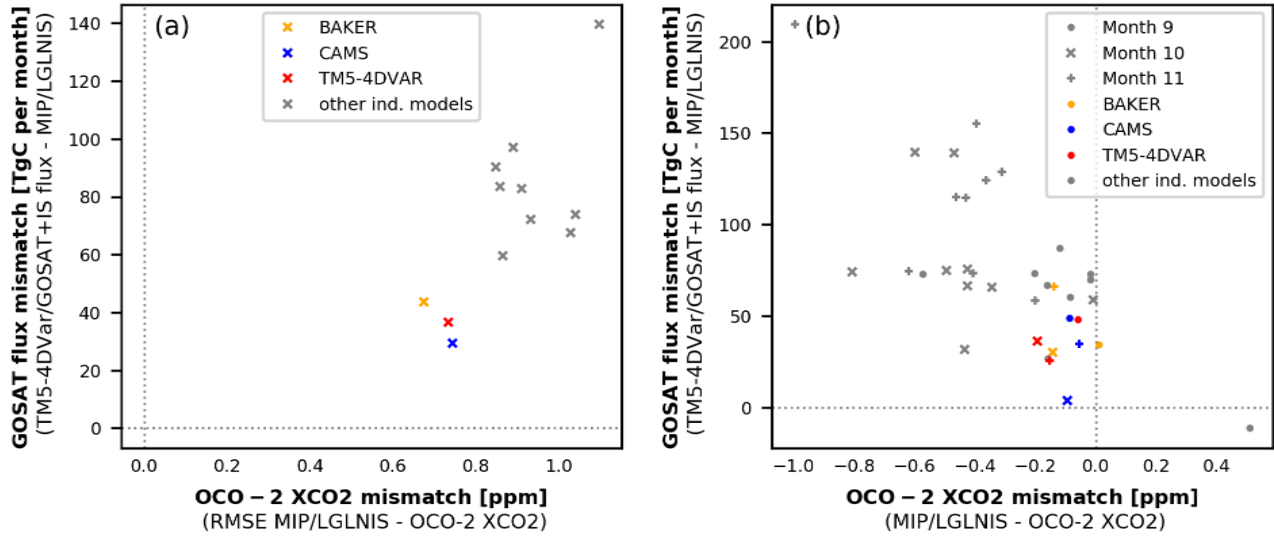
Figure A7: Mismatch between GOSAT-informed and OCO-2 informed fluxes versus mismatch between OCO-2 informed simulated XCO$_2$ and OCO-2 measured XCO$_2$. For the MIP/OCO-2+IS inversions 5% of the OCO-2 measurements are withheld for validation purposes and modelled XCO$_2$ co-sampled on the measurements are provided for each model but CSU. ~~The~~Panel (a) gives the RMSE of the OCO-2 measurements and the modelled co-sampled XCO$_2$ from September to November for each model. In panel (b), the mean differences of the OCO-2 measurements and modelled co-samples for each month and model are given. In both panels, the OCO-2 XCO$_2$ mismatch is plotted against the difference of the monthly TM5-4DVar/GOSAT+IS and individual MIP/OCO-2+IS CO$_2$ ~~flux.~~fluxes for the strongest emission period from September to November. The MIP models Baker, CAMS and TM5-4DVar are highlighted in yellow, blue and red. The other individual MIP models are given in grey. The three highlighted models show the smallest OCO-2 XCO$_2$ mismatch and the smallest difference to the monthly fluxes of TM5-4DVar/GOSAT+IS (exception Baker in September, panel b).

~~Figure A4~~
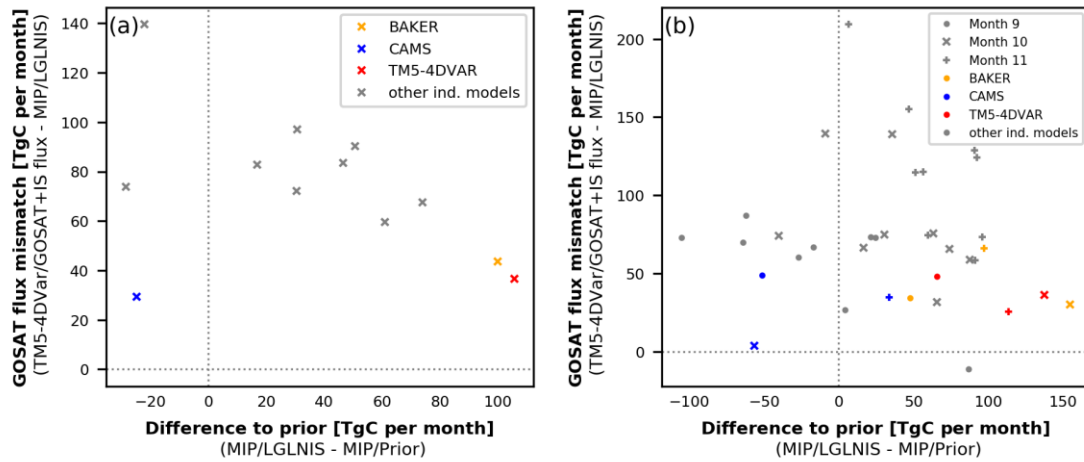
Figure A8: Mismatch between GOSAT-informed and OCO-2 informed fluxes versus difference between OCO-2 informed fluxes and model prior fluxes. The individual MIP models differ in their assumed prior fluxes. In this figure, the differences of the monthly posterior to the prior fluxes (x-axis) and to the GOSAT based fluxes (TM5-4DVar/GOSAT+IS, y-axis) are compared. Differences are calculated using the monthly flux over the whole study region and the time period 2015-2018. Panel (a) shows the mean over September to November, the time of the strongest CO$_2$ emissions. In panel (b), the differences are given for each of the three individual months. The MIP models Baker, CAMS, and TM5-4DVar are highlighted in yellow, blue, and red. The other individual MIP models are given in grey.
For most of the models the assimilation of OCO-2 measurements increases the mean monthly fluxes from September to November (difference to prior larger than zero). Only for CAMS and UT, and for some models in September, the mean posterior fluxes are smaller than the prior fluxes.
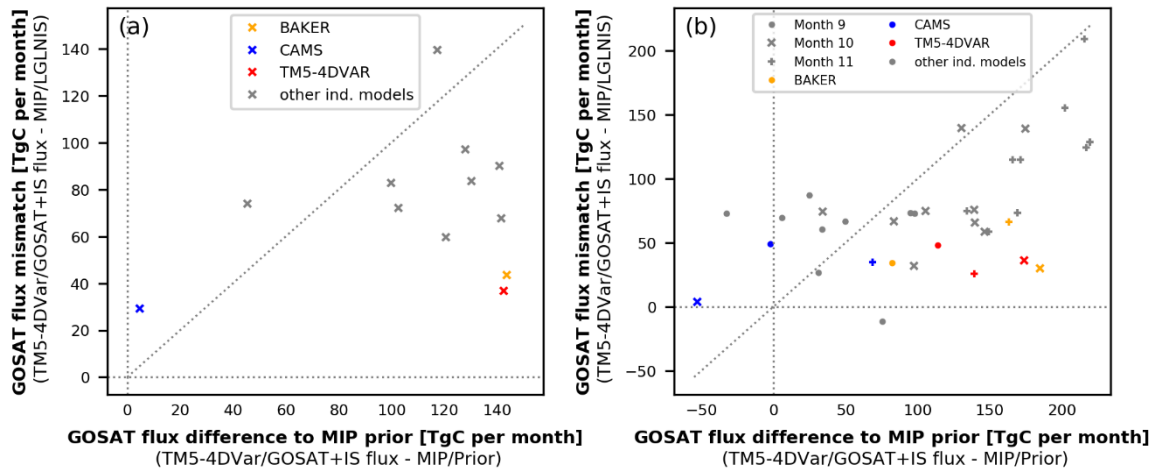
Figure A9: Mismatch between GOSAT-informed and OCO-2 informed fluxes versus difference between GOSAT informed fluxes and OCO-2 MIP prior fluxes. The differences of the monthly GOSAT inversion fluxes (TM5-4DVar/GOSAT+IS) to the MIP posterior (y-axis) and MIP prior fluxes (x-axis) for the individual MIP models is given. Panel (a) gives the mean differences for the months September to November. Panel (b) shows the differences for the individual months. The MIP models Baker, CAMS and TM5-4DVar are highlighted in yellow, blue and red. The other individual MIP models are given in grey. The 1:1 line is given in grey dotted. For most of the MIP models, assimilating OCO-2 reduces the flux difference to the GOSAT based fluxes (i.e. markers are below the 1:1 line).
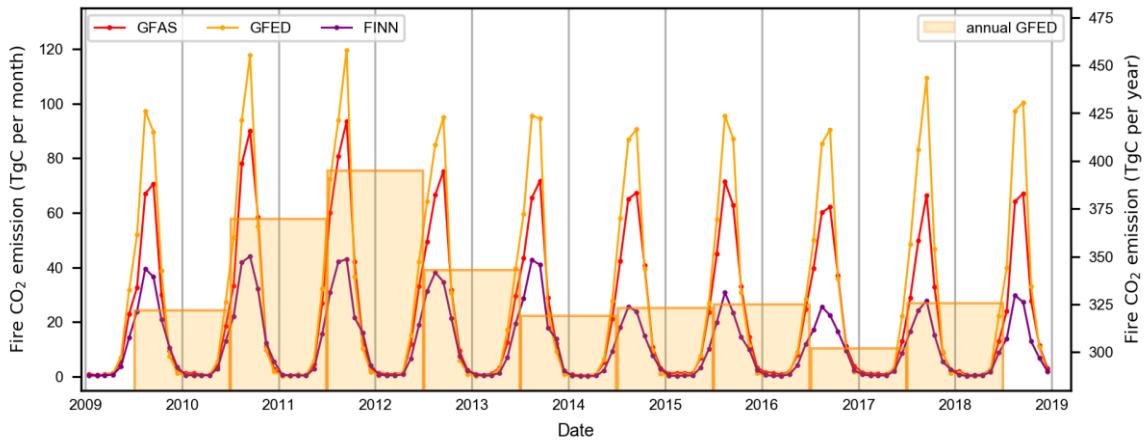
580 **Figure A10**: CO$_2$ **fire emissions in southern Africa. The monthly CO$_2$ fire emissions collected by three fire emission databases (GFED in orange, Global Fire Assimilation System (GFAS (, Kaiser et al., 2012))) in red and the Fire INventory from NCAR (FINN (, Wiedinmyer et al., 2011))) in purple). Furthermore, the annual (July - June) GFED fire emissions are given with the right y-axis. Please note, that the right y-axis starts at 280 TgC per year for better visualization of the fire emissions.**

585
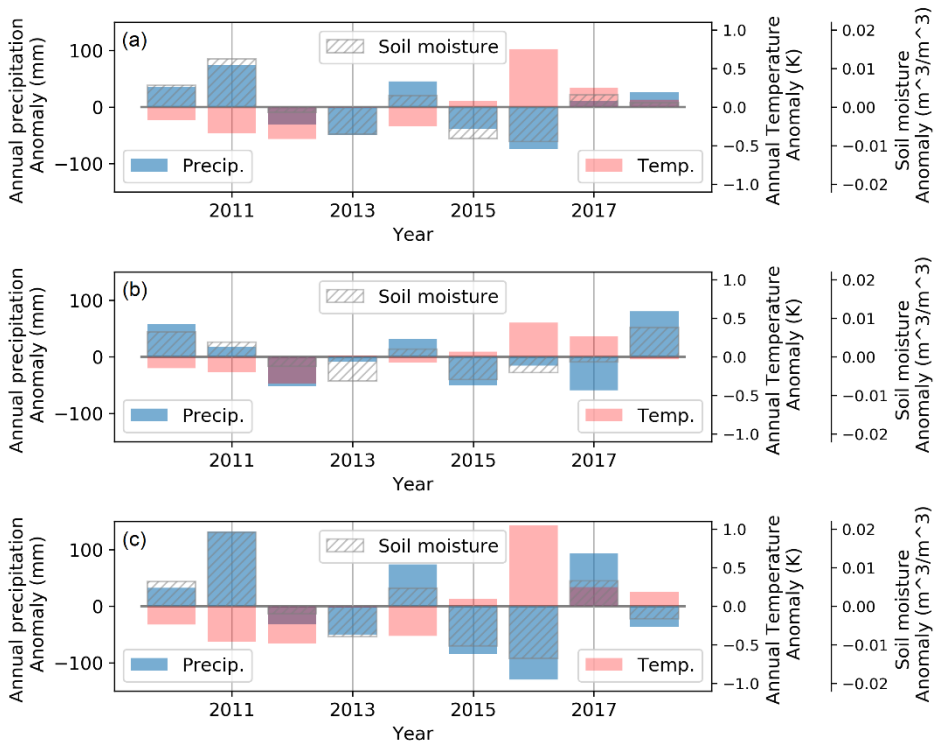
Figure A5A11: Climate Anomalies. The annual anomalies of ERA5 precipitation, temperature and upper layer soil moisture are given in blue, red, and grey hashed. The annual anomalies are calculated by subtracting the individual long-term mean of the annual values. and are given for the whole study region in panel (a), for the northern subregion in panel (b), and southern subregion in panel (c).
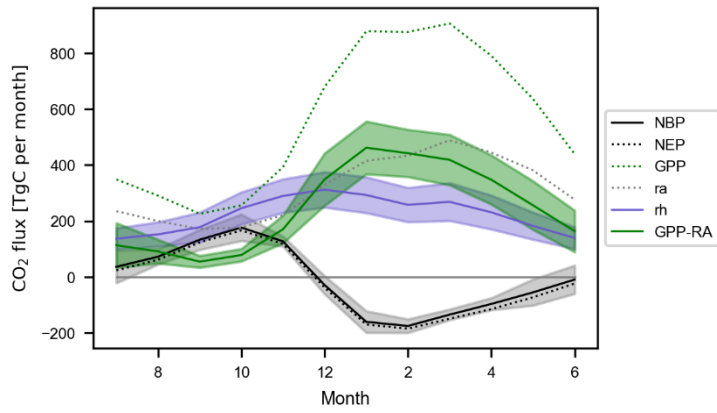
Figure A6A12: Mean monthly CO₂ net and gross fluxes. Like Fig. 8 (a) but additionally with GPP and RA of the TRENDY
595   selection.
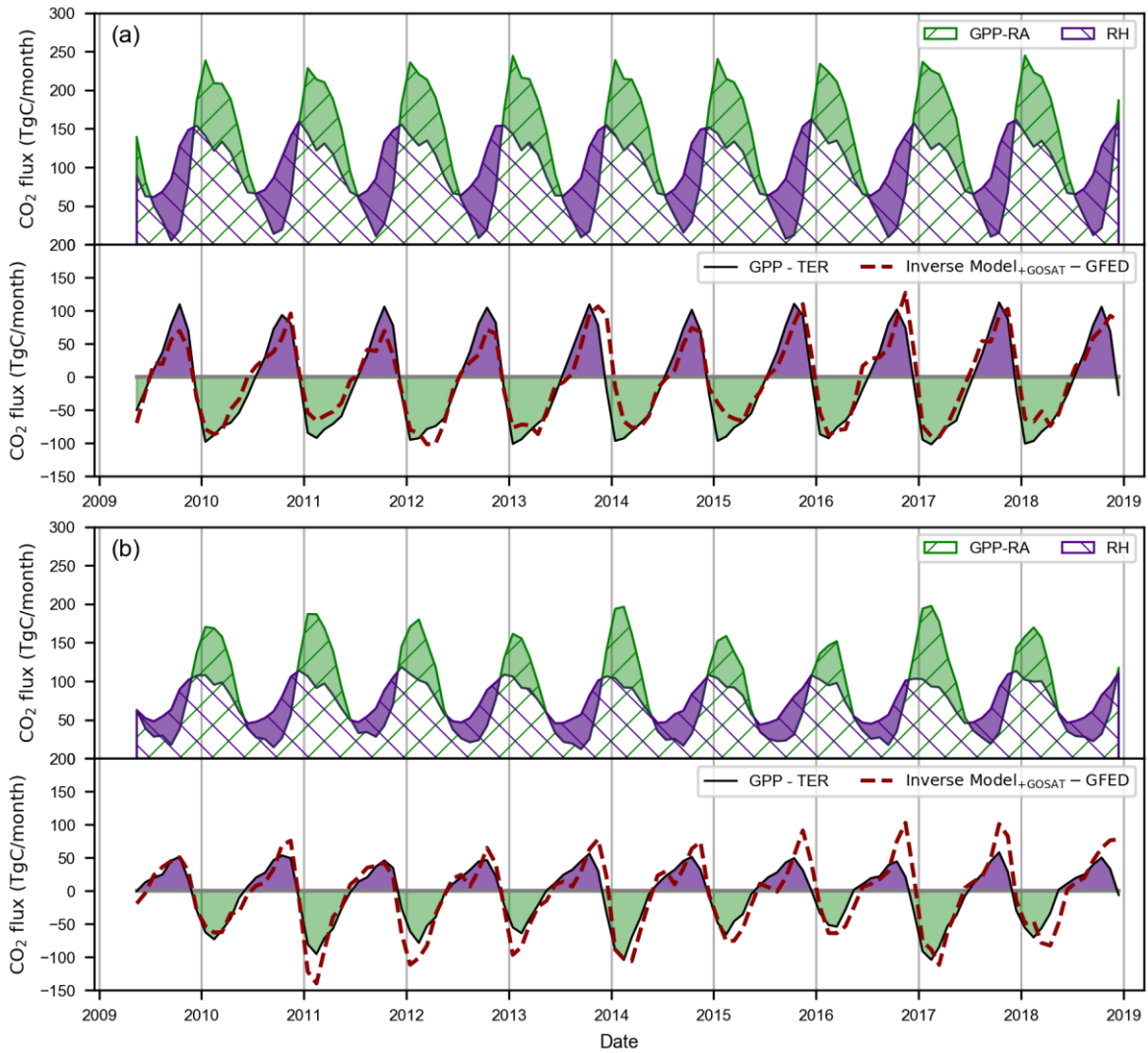
Figure ~~A7~~A13: Monthly CO₂ fluxes in northern (Panel (a)) and southern (Panel (b)) subregion. The monthly NEE, NPP (GPP-RA), and RH fluxes from the selected TRENDY models are given in black, green, and violet respectively for the northern southern African region in Panel (a). The TM5-4DVar/GOSAT+IS - GFED NEE fluxes are additionally shown in red dotted. The same is given in Panel (b) for the southern subregion.

610
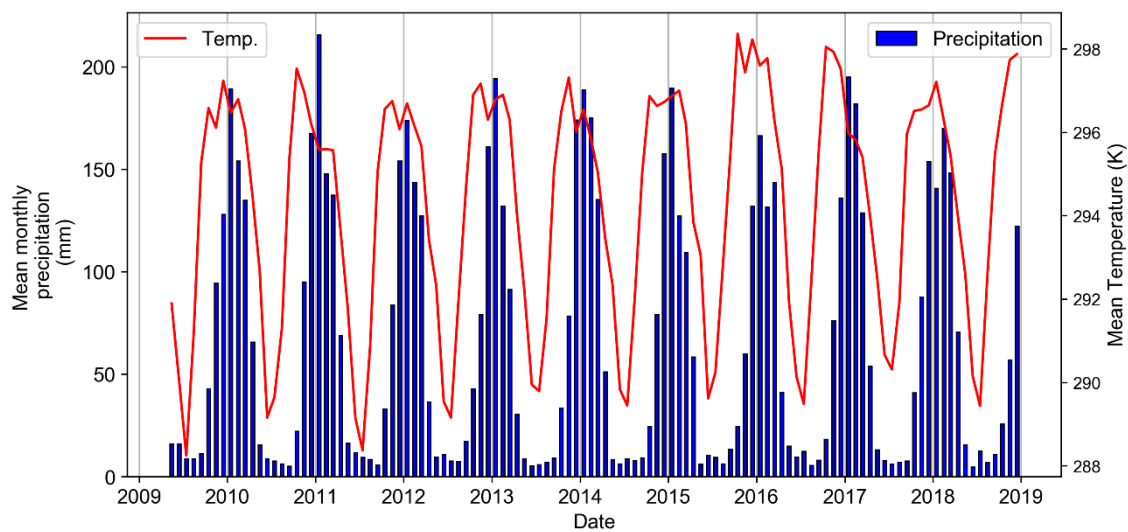
Figure A8A14: Monthly precipitation and temperature as mean over southern Africa. The monthly precipitation is given as blue bars and the mean temperature as solid red line.
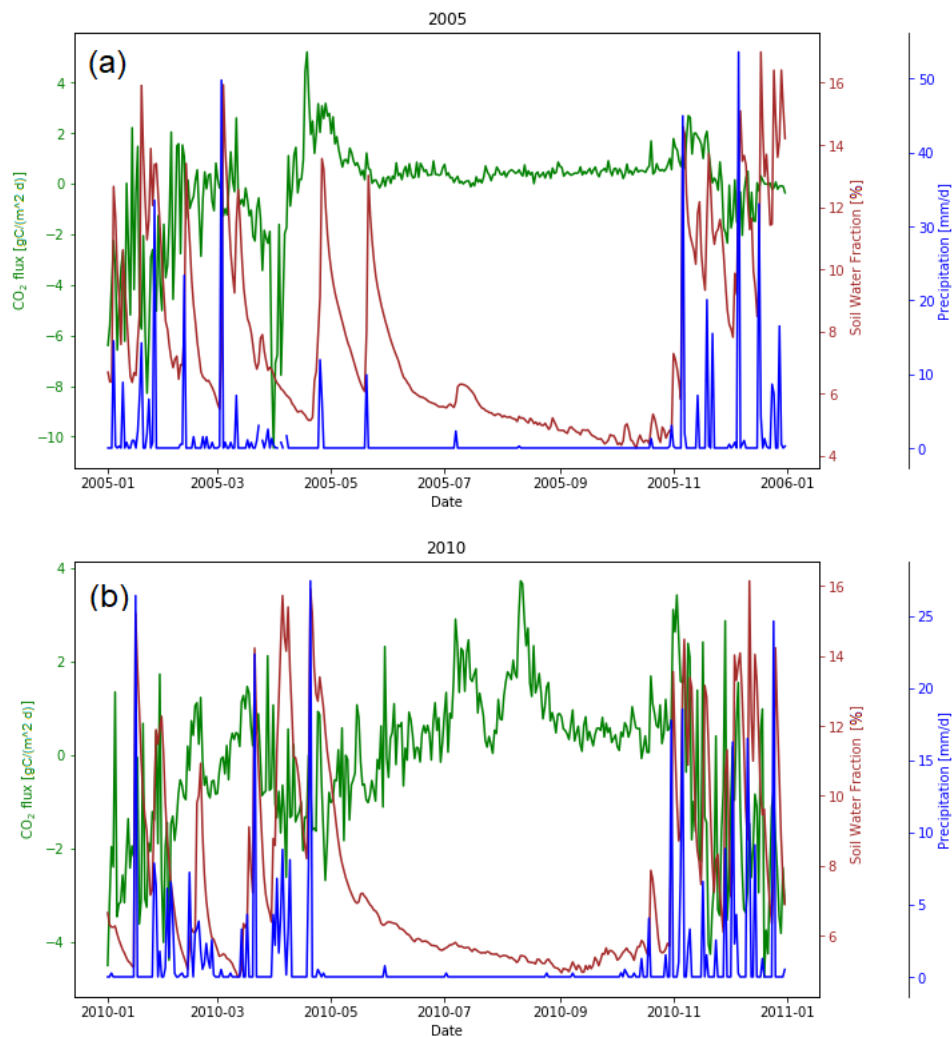
615

Figure A9A15: Local data from FLUXNET eddy covariance flux tower in Kruger National Park. Daily mean net carbon fluxes (green), precipitation (blue) and soil moisture (red) measured by the FLUXNET station ZA-Kru (Archibald et al., 2009). Panel (a) shows the year 2005, Panel (b) shows 2010.

620 Table A1: Summary of datasets

Description	Dataset	Resolution	References
GOSAT XCO$_2$	GOSAT/RemoTeC v2.4.0 GOSAT/ACOS v9r(Lite)	10.5 km footprint 10.5 km footprint	Butz et al., 2011, 2022 Taylor et al., 2022, OCO-2 Science Team, 2019
Validation XCO$_2$	OCO-2 v11r COCCON Gobabeb	1.3×2.3 km footprint local	~~Eldering~~Jacobs et al., ~~2017,~~2024; OCO-2/OCO-3 Science Team, 2020 Frey et al., 2021, Dubravica, et al., 2021
Model XCO$_2$ based on in- situ data	TM5 − 4DVAR/IS CarbonTracker CT2022 CAMS v21r1	3°×2°, monthly 3°×2°, monthly 3.7°×1.81°, monthly	Basu et al., 2013 Peters et al., 2007; Jacobson et al., 2023 Chevallier et al., 2005, 2010, 2019
In-situ-only inversions	TM5 − 4DVAR/IS CarbonTracker CT2022 CAMS v20r1	3°×2°, monthly 1°×1°, monthly 3.7°×1.81°, monthly	Basu et al., 2013 Peters et al., 2007; Jacobson et al., 2023 Chevallier et al., 2005, 2010, 2019
TM5-4DVar/GOSAT+IS	TM5-4DVar/RemoTeC+IS and TM5-4DVar/ACOS+IS	3°x2°, monthly	Basu et al., 2013
TM5-4DVar/OCO-2+IS	TM5-4DVar of MIP/LNLGIS	1°x1°, monthly	Basu et al., 2013; Byrne et al., 2023
MIP/OCO-2+IS MIP/IS	MIP/LNLGIS experiment MIP/IS experiment	1°x1°, monthly	Byrne et al., 2023
SIF	GOME-2 Daily_Averaged_SIF	40 km x 40 km/80 km	Joiner et al., 2023
FLUXCOM + GFED	~~FLUXCOM~~FLUXCOMv1 NEE, RS_V006 GFED v4.1s	0.08°×0.08°, 8-days 0.25°×0.25°, monthly	Tramontana et al., 2016; Jung et al., 2020 Van der Werf et al., 2017
TRENDY$_{selection}$ TRENDY$_{others}$	ORCHIDEE S3 ORCHIDEEv3 S3 CABLE-POP S3 YIBs S3 OCN S3 ORCHIDEE-CNP S3 JSBACH S3 CLASSIC S3 LPJ S3 CLM5.0 S3 DLEM S3 IBIS S3 ISAM S3 ISBA-CTRIP S3 JULES-ES-1.0 S3 LPX-Bern S3 SDGVM S3 VISIT S3	0.5°x0.5° [1] 2°x2° [1] 1°x1° [1] 1°x1° [1] 1°x1° [1] 2°x2° [1] 1.86°x1.88° [1] 2.80°x2.81° [1] 0.5°x0.5° [1] 0.94°x1.25° [1] 0.5°x0.5° [1] 1°x1° [1] 0.5°x0.5° [1] 1°x1° [1] 1.25°x1.88° [1] 0.5°x0.5° [1] 1°x1° [1] 0.5°x0.5° [1]	Krinner et al., 2005 Vuichard et al., 2019 Haverd et al., 2018 Yue and Unger, 2015 Zaehle et al., 2010 Goll et al., 2018 Reick et al., 2021 Melton et al., 2020 Poulter et al., 2011 Lawrence et al., 2019 Tian et al., 2015 Yuan et al., 2014 Meiyppan et al., 2015 Delire et al., 2020 Sellar et al., 2019 Lienert and Joos, 2018 Walker et al., 2017 Kato et al., 2013
ERA5 meteorological data	ERA5-land data total precipitation, upper layer soil moisture, temperature	1°×1°, monthly	Muñoz Sabater 2019, 2021
MODIS	MODIS (MCD12C1) data	0.05°x0.05°, 2015	Friedl and Sulla-Menashe, 2022

[1] all TRENDY model data is provided in monthly temporal resolution

The main characteristics and references of the observation and model data are listed. Links to the datasets are provided in the Data availability section.

Table A2: Monthly fluxes of TM5-4DVar/GOSAT+IS in southern Africa

Year	Month	RT+IS	ACOS+IS	Mean	Year	Month	RT+IS	ACOS+IS	Mean
2009	4	-157.56	-195.50	-176.53	2014	3	-218.74	-194.84	-206.79
2009	5	-83.13	-102.61	-92.87	2014	4	-160.54	-153.89	-157.21
2009	6	6.71	6.29	6.50	2014	5	-84.72	-81.25	-82.99
2009	7	93.92	109.99	101.96	2014	6	30.42	42.46	36.44
2009	8	163.05	163.17	163.11	2014	7	82.04	99.66	90.85
2009	9	219.63	198.25	208.94	2014	8	95.93	122.13	109.03
2009	10	232.99	144.91	188.95	2014	9	215.17	154.74	184.96
2009	11	140.76	88.81	114.79	2014	10	229.27	176.57	202.92
2009	12	-32.79	-44.05	-38.42	2014	11	199.23	168.02	183.62
2010	1	-144.40	-113.34	-128.87	2014	12	36.93	-35.25	0.84
2010	2	-153.14	-157.85	-155.50	2015	1	-73.64	-86.37	-80.01
2010	3	-144.99	-172.86	-158.93	2015	2	-139.19	-135.31	-137.25
2010	4	-74.81	-121.29	-98.05	2015	3	-153.79	-149.43	-151.61
2010	5	-57.83	-84.45	-71.14	2015	4	-144.28	-131.81	-138.04
2010	6	24.59	16.57	20.58	2015	5	-62.78	-63.61	-63.19
2010	7	69.44	86.01	77.73	2015	6	2.16	22.31	12.24
2010	8	129.28	152.92	141.10	2015	7	49.88	85.39	67.64
2010	9	208.69	202.44	205.57	2015	8	117.11	107.91	112.51
2010	10	239.32	194.63	216.98	2015	9	189.95	139.90	164.93
2010	11	262.58	166.15	214.37	2015	10	225.03	150.79	187.91
2010	12	57.84	-24.29	16.78	2015	11	259.19	212.22	235.70
2011	1	-189.14	-146.26	-167.70	2015	12	112.16	78.85	95.50
2011	2	-229.46	-193.03	-211.24	2016	1	-72.92	-69.47	-71.20
2011	3	-156.96	-183.26	-170.11	2016	2	-148.67	-155.69	-152.18
2011	4	-111.27	-115.31	-113.29	2016	3	-176.60	-134.03	-155.32
2011	5	-70.44	-72.17	-71.31	2016	4	-159.32	-128.91	-144.11
2011	6	22.49	39.77	31.13	2016	5	-77.83	-56.86	-67.35
2011	7	88.88	101.56	95.22	2016	6	28.77	72.38	50.58
2011	8	170.18	183.09	176.63	2016	7	61.68	117.42	89.55
2011	9	214.57	202.08	208.32	2016	8	111.76	166.74	139.25
2011	10	215.25	137.67	176.46	2016	9	178.65	176.21	177.43
2011	11	108.61	83.75	96.18	2016	10	278.49	178.25	228.37
2011	12	-69.23	-42.93	-56.08	2016	11	344.93	213.55	279.24
2012	1	-198.76	-174.22	-186.49	2016	12	126.39	48.90	87.64
2012	2	-204.51	-185.68	-195.09	2017	1	-141.60	-144.98	-143.29
2012	3	-201.66	-209.21	-205.43	2017	2	-218.16	-157.23	-187.70
2012	4	-157.34	-149.79	-153.56	2017	3	-266.37	-195.15	-230.76
2012	5	-85.64	-61.66	-73.65	2017	4	-171.98	-145.48	-158.73
2012	6	26.99	55.95	41.47	2017	5	-87.55	-94.62	-91.09
2012	7	81.80	111.87	96.84	2017	6	-4.45	17.30	6.43
2012	8	105.47	131.05	118.26	2017	7	36.00	108.33	72.17
2012	9	182.86	156.69	169.77	2017	8	125.62	175.62	150.62
2012	10	216.78	172.23	194.51	2017	9	191.89	212.30	202.10
2012	11	130.49	155.95	143.22	2017	10	285.32	197.40	241.36
2012	12	-29.84	-24.57	-27.20	2017	11	233.14	175.95	204.54
2013	1	-195.13	-142.42	-168.78	2017	12	3.21	3.05	3.13
2013	2	-181.41	-141.65	-161.53	2018	1	-131.45	-111.65	-121.55
2013	3	-150.87	-134.34	-142.60	2018	2	-119.89	-127.09	-123.49
2013	4	-133.19	-113.00	-123.10	2018	3	-167.60	-135.00	-151.30
2013	5	-72.44	-40.57	-56.51	2018	4	-208.14	-153.04	-180.59
2013	6	34.37	52.38	43.38	2018	5	-137.36	-102.90	-120.13
2013	7	64.78	85.80	75.29	2018	6	-21.20	23.47	1.14
2013	8	96.91	130.53	113.72	2018	7	29.86	98.30	64.08
2013	9	176.64	185.33	180.99	2018	8	110.99	163.25	137.12
2013	10	219.32	178.29	198.80	2018	9	202.02	201.28	201.65
2013	11	249.06	191.11	220.08	2018	10	182.51	179.17	180.84
2013	12	202.08	64.14	133.11	2018	11	223.74	184.91	204.33
2014	1	-79.09	-119.87	-99.48	2018	12	226.30	148.33	187.31
2014	2	-187.16	-169.20	-178.18					

625 The monthly fluxes of TM5-4DVar/RemoTeC+IS ('RT+IS'), TM5-4DVar/ACOS+IS (ACOS+IS), and the mean of both is given in TgC/month for the whole study region.

Data availability. GOSAT/RemoTeC2.4.0 XCO$_2$ data can be obtained from Zenodo https://doi.org/10.5281/zenodo.7648699 (Butz, 2022) (last access: 2024-05-15). GOSAT/ACOS data are available at https://oco2.gesdisc.eosdis.nasa.gov/data/GOSAT_TANSO_Level2/ACOS_L2_Lite_FP.9r/ (last access: 2020-07-28). OCO-2 data are available at https://disc.gsfc.nasa.gov/datasets/OCO2_L2_Standard_11r/summary (last access: 2023-06-28). CarbonTracker CT2022 CO$_2$ fluxes and concentrations can be downloaded from https://gml.noaa.gov/aftp/products/carbontracker/co2/CT2022/fluxes/monthly/ (last access: 2023-04-17) and https://gml.noaa.gov/aftp/products/carbontracker/co2/CT2022/molefractions/co2_total_monthly/ (last access: 2024-06-0709-17), respectively. CAMS concentrations and fluxes can be found at https://ads.atmosphere.copernicus.eu/cdsapp#!/dataset/cams-global-greenhouse-gas-inversion (last access: 2021-10-07). GFAS emissions records are available at https://apps.ecmwf.int/ datasets/data/cams-gfas/ (last access: 2020-11-13). CAMS and GFAS data were generated using Copernicus Atmosphere Service Information [2021], and neither the European Commission nor the European Centre for Medium-Range Weather Forecasts (ECMWF) is responsible for any use that may be made of the information it contains. The MIP data can be downloaded from https://www.gml.noaa.gov/ccgg/OCO2_v10mip/ (last access: 2022-05-06). GFED fire emissions are available at https://www.geo.vu.nl/~gwerf/GFED/GFED4/ (last access: 2020-07-10). FINN data were retrieved from the American National Center for Atmospheric Research https://www2.acom.ucar.edu/modeling/finn-fire-inventory-ncar (last access: 2020-11-18). ERA5-land data records contain modified Copernicus Atmosphere Service Information [2021] available at the Climate Data Store https://cds.climate.copernicus.eu/cdsapp#!/dataset/reanalysis-era5-land-monthly-means (last access: 2023-10-13). TRENDYv9 model output and FLUXCOM products are available at https://sites.exeter.ac.uk/trendy and http://fluxcom.org/CF-Download/, respectively. Data of the FLUXNET station ZA-Kru can be downloaded from the FLUXNET webpage: https://fluxnet.org/data/fluxnet2015-dataset/ (last access 21.11.2023). COCCON Gobabeb station data is available at https://secondary-data-archive.nilu.no/evdc/ftir/coccon/gobabeb/version2/ (last access: 2023-03-27). MODIS MCD12C1 data is available on https://search.earthdata.nasa.gov/search with the DOI 10.5067/MODIS/MCD12C1.061 (last access: 2024-03-24). L2 Daily Solar-Induced Fluorescence (SIF) from MetOp-A GOME-2 V2 data is available at from https://search.earthdata.nasa.gov/ (last access 2024-05-29). Monthly TM5-4DVAR data are available in Table A2.

Code availability: The code used in this study is available at https://zenodo.org/doi/10.5281/zenodo.12528504 or GitHub (https://github.com/ ATMO-IUP-UHEI/MetzEtAl2024)

Competing interests. The authors declare that they have no conflict of interest.

Author contributions. S.N.V., A.B. and E.-M.M. were involved in conceptualization and methodology. S.B. performed the dedicated TM5-4DVAR runs. E.-M.M. conducted the formal analysis and the visualization under the supervision of A.B.

and S.N.V. E.-M.M. wrote the original draft. All authors contributed to the interpretation of the results and the editing and review of the manuscript.

Funding. Funding for the developing RemoTeC was provided by the German Research Foundation (DFG) through grant
665 BU2599/1-1, operations and data storage was supported by DFG grant INST 35/1503-1 FUGG. S.B. was supported by NASA grant 80NSSC20K0818.

Acknowledgements. We gratefully acknowledge the data storage service SDS@hd supported by the Ministry of Science, Research and the Arts Baden-Württemberg (MWK) and the computing resources provided by the DKRZ under
670 project bb1170. E.-M.M. acknowledges a doctoral scholarship from the German National Academic Foundation. We thank the Japanese Aerospace Exploration Agency, the National Institute for Environmental Studies, and the Ministry of Environment for the GOSAT data and their continuous support as part of the Joint Research Agreement. We thank the OCO-2 science team for producing the GOSAT/ACOS L2 XCO_2 data. OCO-2 data were produced by the OCO-2 project at the Jet Propulsion Laboratory, California Institute of Technology, and obtained from the OCO-2 data archive maintained at the
675 NASA Goddard Earth Science Data and Information Services Center. CarbonTracker CT2022 results were provided by NOAA ESRL, Boulder, Colorado, USA, from the website at http://carbontracker.noaa.gov. We thank Stephen Sitch, Pierre Friedlingstein, and all modellers of the Trends in Net Land-Atmosphere Exchange project (TRENDY; https://blogs.exeter.ac.uk/trendy/). The long-term operation of the COCCON Gobabeb site in Namibia is supported by ESA via the COCCON-PROCEEDS series of projects (contract no. 4000121212) and COCCON-OPERA (contract no.
680 4000140431/23/I-DT-Ir).

References

Ahlström, A., Raupach, M. R., Schurgers, G., Smith, B., Arneth, A., Jung, M., Reichstein, M., Canadell, J. G., Friedlingstein, P., Jain, A. K., Kato, E., Poulter, B., Sitch, S., Stocker, B. D., Viovy, N., Wang, Y. P., Wiltshire, A.,
685   Zaehle, S., and Zeng, N.: The dominant role of semi-arid ecosystems in the trend and variability of the land CO_2 sink, Science, 348, 895–899, doi:10.1126/science.aaa1668, 2015.

Archibald, S. A., Kirton, A., van der Merwe, M. R., Scholes, R. J., Williams, C. A., and Hanan, N.: Drivers of inter-annual variability in Net Ecosystem Exchange in a semi-arid savanna ecosystem, South Africa, Biogeosciences, 6, 251–266, doi:10.5194/bg-6-251-2009, 2009.

690   Bastos, A., O'Sullivan, M., Ciais, P., Makowski, D., Sitch, S., Friedlingstein, P., Chevallier, F., Rödenbeck, C., Pongratz, J., Luijkx, I. T., Patra, P. K., Peylin, P., Canadell, J. G., Lauerwald, R., Li, W., Smith, N. E., Peters, W., Goll, D. S., Jain, A. K., Kato, E., Lienert, S., Lombardozzi, D. L., Haverd, V., Nabel, J. E. M. S., Poulter, B., Tian, H., Walker, A. P., and Zaehle, S.: Sources of Uncertainty in Regional and Global Terrestrial CO_2 Exchange Estimates, Global Biogeochem. Cycles, 34, e2019GB006393, doi:10.1029/2019GB006393, 2020.

695   Basu, S., Guerlet, S., Butz, A., Houweling, S., Hasekamp, O., Aben, I., Krummel, P., Steele, P., Langenfelds, R., Torn, M., Biraud, S., Stephens, B., Andrews, A., and Worthy, D.: Global CO_2 fluxes estimated from GOSAT retrievals of total column CO_2: exit, Atmos. Chem. Phys., 13, 8695–8717, doi:10.5194/acp-13-8695-2013, 2013.

Birch, H. F.: Mineralisation of plant nitrogen following alternate wet and dry conditions, Plant Soil, 20, 43–49, doi:10.1007/bf01378096, 1964.

700   Buchwitz, M., Reuter, M., Schneising, O., Hewson, W., Detmers, R. G., Boesch, H., Hasekamp, O. P., Aben, I., Bovensmann, H., Burrows, J. P., Butz, A., Chevallier, F., Dils, B., Frankenberg, C., Heymann, J., Lichtenberg, G., Mazière, M. de, Notholt, J., Parker, R., Warneke, T., Zehner, C., Griffith, D., Deutscher, N. M., Kuze, A., Suto, H., and Wunch, D.: Global satellite observations of column-averaged carbon dioxide and methane: The GHG-CCI XCO2 and XCH4 CRDP3 data set, Remote Sensing of Environment, 203, 276–295, doi:10.1016/j.rse.2016.12.027, 2017.

705   Butz, A., Guerlet, S., Hasekamp, O., Schepers, D., Galli, A., Aben, I., Frankenberg, C., Hartmann, J.-M., Tran, H., Kuze, A., Keppel-Aleks, G., Toon, G., Wunch, D., Wennberg, P., Deutscher, N., Griffith, D., Macatangay, R., Messerschmidt, J., Notholt, J., and Warneke, T.: Toward accurate CO_2 and CH_4 observations from GOSAT, Geophys. Res. Lett., 38, n/a-n/a, doi:10.1029/2011GL047888, 2011.

Butz, A.: RemoTeC full-physics retrieval GOSAT/TANSO-FTS Level 2 bias-corrected XCO_2 version 2.4.0 operated at
710   Heidelberg University [data set], doi:10.5281/zenodo.5886662, 2022.

Byrne, B., Baker, D. F., Basu, S., Bertolacci, M., Bowman, K. W., Carroll, D., Chatterjee, A., Chevallier, F., Ciais, P., Cressie, N., Crisp, D., Crowell, S., Deng, F., Deng, Z., Deutscher, N. M., Dubey, M. K., Feng, S., García, O. E., Griffith, D. W. T., Herkommer, B., Hu, L., Jacobson, A. R., Janardanan, R., Jeong, S., Johnson, M. S., Jones, D. B. A., Kivi, R., Liu, J., Liu, Z., Maksyutov, S., Miller, J. B., Miller, S. M., Morino, I., Notholt, J., Oda, T., O'Dell, C. W., Oh, Y.-S.,

715   Ohyama, H., Patra, P. K., Peiro, H., Petri, C., Philip, S., Pollard, D. F., Poulter, B., Remaud, M., Schuh, A., Sha, M. K., Shiomi, K., Strong, K., Sweeney, C., Té, Y., Tian, H., Velazco, V. A., Vrekoussis, M., Warneke, T., Worden, J. R., Wunch, D., Yao, Y., Yun, J., Zammit-Mangion, A., and Zeng, N.: National CO_2 budgets (2015–2020) inferred from atmospheric CO_2 observations in support of the global stocktake, Earth Syst. Sci. Data, 15, 963–1004, doi:10.5194/essd-15-963-2023, 2023.

720   Chevallier, F., Engelen, R. J., and Peylin, P.: The contribution of AIRS data to the estimation of CO_2 sources and sinks, Geophys. Res. Lett., 32, doi:10.1029/2005GL024229, 2005.

Chevallier, F., Ciais, P., Conway, T. J., Aalto, T., Anderson, B. E., Bousquet, P., Brunke, E. G., Ciattaglia, L., Esaki, Y., and Fröhlich, M.: CO_2 surface fluxes at grid point scale estimated from a global 21 year reanalysis of atmospheric measurements, J. Geophys. Res. Atmos., 115, doi:10.1029/2010JD013887, 2010.

725   Chevallier, F., Remaud, M., O'Dell, C. W., Baker, D., Peylin, P., and Cozic, A.: Objective evaluation of surface- and satellite-driven carbon dioxide atmospheric inversions, Atmos. Chem. Phys., 19, 14233–14251, doi:10.5194/acp-19-14233-2019, 2019.

Ciais, P., Piao, S.-L., Cadule, P., Friedlingstein, P., and Chédin, A.: Variability and recent trends in the African terrestrial carbon balance, Biogeosciences, 6, 1935–1948, doi:10.5194/bg-6-1935-2009, 2009.

730   Delire, C., Séférian, R., Decharme, B., Alkama, R., Calvet, J.-C., Carrer, D., Gibelin, A.-L., Joetzjer, E., Morel, X., Rocher, M., and Tzanos, D.: The Global Land Carbon Cycle Simulated With ISBA-CTRIP: Improvements Over the Last Decade, J. Adv. Model. Earth Syst., 12, doi:10.1029/2019MS001886, 2020.

Detmers, R. G., Hasekamp, O., Aben, I., Houweling, S., Leeuwen, T. T., Butz, A., Landgraf, J., Köhler, P., Guanter, L., and Poulter, B.: Anomalous carbon uptake in Australia as seen by GOSAT, Geophys. Res. Lett., 42, 8177–8184,

735   doi:10.1002/2015GL065161, 2015.

Dubravica, D., Hase, F., Alberti, C., Frey, M., Marais, E.: COCCON Version 2 dataset from atmospheric observatory of Gobabeb (Namibia) available at the EVDC Data Handling Facilities covering start date Jan 9th 2017 to end date Nov 27th 2020, COCCON - Central Facility / EVDC - ESA Atmospheric Validation Data Centre [data set], doi:10.48477/coccon.pfl0.gobabeb.R02, 2021.

740   Edwards, D. P., Emmons, L. K., Gille, J. C., Chu, A., Attié, J.-L., Giglio, L., Wood, S. W., Haywood, J., Deeter, M. N., Massie, S. T., Ziskin, D. C., and Drummond, J. R.: Satellite-observed pollution from Southern Hemisphere biomass burning, J. Geophys. Res., 111, doi:10.1029/2005JD006655, 2006.

~~Eldering, A., Wennberg, P. O., Crisp, D., Schimel, D. S., Gunson, M. R., Chatterjee, A., Liu, J., Schwandner, F. M., Sun, Y., O'Dell, C. W., Frankenberg, C., Taylor, T., Fisher, B., Osterman, G. B., Wunch, D., Hakkarainen, J., Tamminen, J., and~~

745   ~~Weir, B.: The Orbiting Carbon Observatory-2 early science investigations of regional carbon dioxide fluxes, Science, 358, eaam5745, doi:10.1126/science.aam5745, 2017.~~

Ernst, Y., Archibald, S., Balzter, H., Chevallier, F., Ciais, P., Fischer, C. G., Gaubert, B., Higginbottom, T., Higgins, S., Lawal, S., Lacroix, F., Lauerwald, R., Lourenco, M., Martens, C., Mengistu, A. G., Merbold, L., Mitchard, E., Moyo,

M., Nguyen, H., O'sullivan, M., Rodríguez-Veiga, P., Rosan, T., Rosentreter, J., Ryan, C., Scheiter, S., Sitch, S., Stevens, N., Tagesson, T., Tian, H., Wang, M., Woon, J. S., Zheng, B., Zhou, Y., and Scholes, R. J.: The African Regional Greenhouse Gases Budget (2010–2019), Global Biogeochem. Cycles, 38, doi:10.1029/2023GB008016, 2024.

Fan, Z., Neff, J. C., and Hanan, N. P.: Modeling pulsed soil respiration in an African savanna ecosystem, Agricultural and Forest Meteorology, 200, 282–292, doi:10.1016/j.agrformet.2014.10.009, 2015.

Foster, K. T., Sun, W., Shiga, Y. P., Mao, J., and Michalak, A. M.: Multiscale assessment of North American terrestrial carbon balance, Biogeosciences, 21, 869–891, doi:10.5194/bg-21-869-2024, 2024.

Frey, M., Sha, M. K., Hase, F., Kiel, M., Blumenstock, T., Harig, R., Surawicz, G., Deutscher, N. M., Shiomi, K., Franklin, J. E., Bösch, H., Chen, J., Grutter, M., Ohyama, H., Sun, Y., Butz, A., Mengistu Tsidu, G., Ene, D., Wunch, D., Cao, Z., Garcia, O., Ramonet, M., Vogel, F., and Orphal, J.: Building the COllaborative Carbon Column Observing Network (COCCON): long-term stability and ensemble performance of the EM27/SUN Fourier transform spectrometer, Atmos. Meas. Tech., 12, 1513–1530, doi:10.5194/amt-12-1513-2019, 2019.

Frey, M. M., Hase, F., Blumenstock, T., Dubravica, D., Groß, J., Göttsche, F., Handjaba, M., Amadhila, P., Mushi, R., Morino, I., Shiomi, K., Sha, M. K., Mazière, M. de, and Pollard, D. F.: Long-term column-averaged greenhouse gas observations using a COCCON spectrometer at the high-surface-albedo site in Gobabeb, Namibia, Atmos. Meas. Tech., 14, 5887–5911, doi:10.5194/amt-14-5887-2021, 2021.

Friedl, M. and Sulla-Menashe, D.: MODIS/Terra+Aqua Land Cover Type Yearly L3 Global 0.05Deg CMG V061, NASA EOSDIS Land Processes Distributed Active Archive Center [data set], doi:10.5067/MODIS/MCD12C1.061, 2022.

Friedlingstein, P., O'sullivan, M., Jones, M. W., Andrew, R. M., Hauck, J., Olsen, A., Peters, G. P., Peters, W., Pongratz, J., Sitch, S., Le Quéré, C., Canadell, J. G., Ciais, P., Jackson, R. B., Alin, S., Aragão, Luiz E. O. C., Arneth, A., Arora, V., Bates, N. R., Becker, M., Benoit-Cattin, A., Bittig, H. C., Bopp, L., Bultan, S., Chandra, N., Chevallier, F., Chini, L. P., Evans, W., Florentie, L., Forster, P. M., Gasser, T., Gehlen, M., Gilfillan, D., Gkritzalis, T., Gregor, L., Gruber, N., Harris, I., Hartung, K., Haverd, V., Houghton, R. A., Ilyina, T., Jain, A. K., Joetzjer, E., Kadono, K., Kato, E., Kitidis, V., Korsbakken, J. I., Landschützer, P., Lefèvre, N., Lenton, A., Lienert, S., Liu, Z., Lombardozzi, D., Marland, G., Metzl, N., Munro, D. R., Nabel, Julia E. M. S., Nakaoka, S.-I., Niwa, Y., O'Brien, K., Ono, T., Palmer, P. I., Pierrot, D., Poulter, B., Resplandy, L., Robertson, E., Rödenbeck, C., Schwinger, J., Séférian, R., Skjelvan, I., Smith, A. J. P., Sutton, A. J., Tanhua, T., Tans, P. P., Tian, H., Tilbrook, B., van der Werf, G., Vuichard, N., Walker, A. P., Wanninkhof, R., Watson, A. J., Willis, D., Wiltshire, A. J., Yuan, W., Yue, X., and Zaehle, S.: Global Carbon Budget 2020, Earth Syst. Sci. Data, 12, 3269–3340, doi:10.5194/essd-12-3269-2020, 2020.

Friedlingstein, P., O'Sullivan, M., Jones, M. W., Andrew, R. M., Bakker, D. C. E., Hauck, J., Landschützer, P., Le Quéré, C., Luijkx, I. T., Peters, G. P., Peters, W., Pongratz, J., Schwingshackl, C., Sitch, S., Canadell, J. G., Ciais, P., Jackson, R. B., Alin, S. R., Anthoni, P., Barbero, L., Bates, N. R., Becker, M., Bellouin, N., Decharme, B., Bopp, L., Brasika, I. B. M., Cadule, P., Chamberlain, M. A., Chandra, N., Chau, T.-T.-T., Chevallier, F., Chini, L. P., Cronin, M., Dou, X., Enyo, K., Evans, W., Falk, S., Feely, R. A., Feng, L., Ford, D. J., Gasser, T., Ghattas, J., Gkritzalis, T., Grassi, G.,

Gregor, L., Gruber, N., Gürses, Ö., Harris, I., Hefner, M., Heinke, J., Houghton, R. A., Hurtt, G. C., Iida, Y., Ilyina, T., Jacobson, A. R., Jain, A., Jarníková, T., Jersild, A., Jiang, F., Jin, Z., Joos, F., Kato, E., Keeling, R. F., Kennedy, D., Klein Goldewijk, K., Knauer, J., Korsbakken, J. I., Körtzinger, A., Lan, X., Lefèvre, N., Li, H., Liu, J., Liu, Z., Ma, L., Marland, G., Mayot, N., McGuire, P. C., McKinley, G. A., Meyer, G., Morgan, E. J., Munro, D. R., Nakaoka, S.-I., Niwa, Y., O'Brien, K. M., Olsen, A., Omar, A. M., Ono, T., Paulsen, M., Pierrot, D., Pocock, K., Poulter, B., Powis, C. M., Rehder, G., Resplandy, L., Robertson, E., Rödenbeck, C., Rosan, T. M., Schwinger, J., Séférian, R., Smallman, T. L., Smith, S. M., Sospedra-Alfonso, R., Sun, Q., Sutton, A. J., Sweeney, C., Takao, S., Tans, P. P., Tian, H., Tilbrook, B., Tsujino, H., Tubiello, F., van der Werf, G. R., van Ooijen, E., Wanninkhof, R., Watanabe, M., Wimart-Rousseau, C., Yang, D., Yang, X., Yuan, W., Yue, X., Zaehle, S., Zeng, J., and Zheng, B.: Global Carbon Budget 2023, Earth Syst. Sci. Data, 15, 5301–5369, doi:10.5194/essd-15-5301-2023, 2023.

Goll, D. S., Joetzjer, E., Huang, M., and Ciais, P.: Low Phosphorus Availability Decreases Susceptibility of Tropical Primary Productivity to Droughts, Geophys. Res. Lett., 45, 8231–8240, doi:10.1029/2018GL077736, 2018.

Haverd, V., Smith, B., Nieradzik, L., Briggs, P. R., Woodgate, W., Trudinger, C. M., Canadell, J. G., and Cuntz, M.: A new version of the CABLE land surface model (Subversion revision r4601) incorporating land use and land cover change, woody vegetation demography, and a novel optimisation-based approach to plant coordination of photosynthesis, Geosci. Model Dev., 11, 2995–3026, doi:10.5194/gmd-11-2995-2018, 2018.

He, W., Jiang, F., Ju, W., Byrne, B., Xiao, J., Nguyen, N. T., Wu, M., Wang, S., Wang, J., Rödenbeck, C., Li, X., Scholze, M., Monteil, G., Wang, H., Zhou, Y., He, Q., and Chen, J. M.: Do State-Of-The-Art Atmospheric CO_2 Inverse Models Capture Drought Impacts on the European Land Carbon Uptake?, J. Adv. Model. Earth Syst., 15, doi:10.1029/2022MS003150, 2023.

Jacobson, A. R., Schuldt, K. N., Tans, P., Arlyn Andrews, Miller, J. B., Oda, T., Mund, J., Weir, B., Ott, L., Aalto, T., Abshire, J. B., Aikin, K., Aoki, S., Apadula, F., Arnold, S., Baier, B., Bartyzel, J., Beyersdorf, A., Biermann, T., Biraud, S. C., Boenisch, H., Brailsford, G., Brand, W. A., Chen, G., Huilin Chen, Lukasz Chmura, Clark, S., Colomb, A., Commane, R., Conil, S., Couret, C., Cox, A., Cristofanelli, P., Cuevas, E., Curcoll, R., Daube, B., Davis, K. J., Wekker, S. de, Della Coletta, J., Delmotte, M., DiGangi, E., DiGangi, J. P., Di Sarra, A. G., Dlugokencky, E., Elkins, J. W., Emmenegger, L., Shuangxi Fang, Fischer, M. L., Forster, G., Frumau, A., Galkowski, M., Gatti, L. V., Gehrlein, T., Gerbig, C., Francois Gheusi, Gloor, E., Gomez-Trueba, V., Goto, D., Griffis, T., Hammer, S., Hanson, C., Haszpra, L., Hatakka, J., Heimann, M., Heliasz, M., Hensen, A., Hermansen, O., Hintsa, E., Holst, J., Ivakhov, V., Jaffe, D. A., Jordan, A., Joubert, W., Karion, A., Kawa, S. R., Kazan, V., Keeling, R. F., Keronen, P., Kneuer, T., Kolari, P., Kateřina Komínková, Kort, E., Kozlova, E., Krummel, P., Kubistin, D., Labuschagne, C., Lam, D. H., Lan, X., Langenfelds, R. L., Laurent, O., Laurila, T., Lauvaux, T., Lavric, J., Law, B. E., Lee, J., Lee, O. S., Lehner, I., Lehtinen, K., Leppert, R., Leskinen, A., Leuenberger, M., Levin, I., Levula, J., Lin, J., Lindauer, M., Loh, Z., Lopez, M., Luijkx, I. T., Lunder, C. R., Machida, T., Mammarella, I., Manca, G., Manning, A., Manning, A., Marek, M. V., Martin, M. Y., Matsueda, H., McKain, K., Meijer, H., Meinhardt, F., Merchant, L., N. Mihalopoulos, Miles, N. L., Miller, C. E., Mitchell, L., Mölder,

M., Montzka, S., Moore, F., Moossen, H., Morgan, E., Josep-Anton Morgui, Morimoto, S., Müller-Williams, J., J. William Munger, Munro, D., Myhre, C. L., Shin-Ichiro Nakaoka, Jaroslaw Necki, Newman, S., Nichol, S., Niwa, Y., Obersteiner, F., O'Doherty, S., Paplawsky, B., Peischl, J., Peltola, O., Piacentino, S., Jean-Marc Pichon, Pickers, P.,

820   Piper, S., Pitt, J., Plass-Dülmer, C., Platt, S. M., Prinzivalli, S., Ramonet, M., Ramos, R., Reyes-Sanchez, E., Richardson, S. J., Riris, H., Rivas, P. P., Ryerson, T., Saito, K., Sargent, M., Sasakawa, M., Scheeren, B., Schuck, T., Schumacher, M., Seifert, T., Sha, M. K., Shepson, P., Shook, M., Sloop, C. D., Smith, P., Stanley, K., Steinbacher, M., Stephens, B., Sweeney, C., Thoning, K., Timas, H., Torn, M., Tørseth, K., Trisolino, P., Turnbull, J., van den Bulk, P., van Dinther, D., Vermeulen, A., Viner, B., Vitkova, G., Walker, S., Watson, A., Wofsy, S. C., Worsey, J., Worthy, D.,

825   Dickon Young, Zaehle, S., Zahn, A., and Miroslaw Zimnoch: CarbonTracker CT2022, doi:10.25925/z1gj-3254, 2023.

Jacobs, N., O'Dell, C. W., Taylor, T. E., Logan, T. L., Byrne, B., Kiel, M., Kivi, R., Heikkinen, P., Merrelli, A., Payne, V., and Chatterjee, A.: The importance of digital elevation model accuracy in X CO 2 retrievals: improving the Orbiting Carbon Observatory 2 Atmospheric Carbon Observations from Space version 11 retrieval product, Atmos. Meas. Tech., 17, 1375-1401, https://doi.org/10.5194/amt-17-1375-2024, 2024.

830   Jarvis, P., Rey, A., Petsikos, C., Wingate, L., Rayment, M., Pereira, J., Banza, J., David, J., Miglietta, F., Borghetti, M., Manca, G., and Valentini, R.: Drying and wetting of Mediterranean soils stimulates decomposition and carbon dioxide emission: the "Birch effect", Tree Physiol. (Tree Physiology), 27, 929–940, doi:10.1093/treephys/27.7.929, 2007.

Joiner, J., Yoshida, Y., Zhang, Y., Duveiller, G., Jung, M., Lyapustin, A., Wang, Y., and Tucker, C. J.: Estimation of Terrestrial Global Gross Primary Production (GPP) with Satellite Data-Driven Models and Eddy Covariance Flux Data,

835   Remote Sensing, 10, 1346, doi:10.3390/rs10091346, 2018.

Joiner, J., Yoshida, Y., Koehler, P., Frankenberg, C., and Parazoo, N. C.: L2 Daily Solar-Induced Fluorescence (SIF) from MetOp-A GOME-2, 2007-2018, V2, ORNL DAAC, Oak Ridge, Tennessee, USA [data set], doi:10.3334/ORNLDAAC/2292, 2023.

Jung, M., Schwalm, C., Migliavacca, M., Walther, S., Camps-Valls, G., Koirala, S., Anthoni, P., Besnard, S., Bodesheim, P.,

840   Carvalhais, N., Chevallier, F., Gans, F., Goll, D. S., Haverd, V., Köhler, P., Ichii, K., Jain, A. K., Liu, J., Lombardozzi, D., Nabel, Julia E. M. S., Nelson, J. A., O'Sullivan, M., Pallandt, M., Papale, D., Peters, W., Pongratz, J., Rödenbeck, C., Sitch, S., Tramontana, G., Walker, A., Weber, U., and Reichstein, M.: Scaling carbon fluxes from eddy covariance sites to globe: synthesis and evaluation of the FLUXCOM approach, Biogeosciences, 17, 1343–1365, doi:10.5194/bg-17-1343-2020, 2020.

845   Kaiser, J. W., Heil, A., Andreae, M. O., Benedetti, A., Chubarova, N., Jones, L., Morcrette, J.-J., Razinger, M., Schultz, M. G., Suttie, M., and van der Werf, G. R.: Biomass burning emissions estimated with a global fire assimilation system based on observed fire radiative power, Biogeosciences, 9, 527–554, doi:10.5194/bg-9-527-2012, 2012.

Kato, E., Kinoshita, T., Ito, A., Kawamiya, M., and Yamagata, Y.: Evaluation of spatially explicit emission scenario of land-use change and biomass burning using a process-based biogeochemical model, Journal of Land Use Science, 8, 104–

850   122, doi:10.1080/1747423X.2011.628705, 2013.

Krinner, G., Viovy, N., Noblet-Ducoudré, N. de, Ogée, J., Polcher, J., Friedlingstein, P., Ciais, P., Sitch, S., and Prentice, I. C.: A dynamic global vegetation model for studies of the coupled atmosphere-biosphere system, Global Biogeochem. Cycles, 19, doi:10.1029/2003GB002199, 2005.

Lasslop, G., Hantson, S., Harrison, S. P., Bachelet, D., Burton, C., Forkel, M., Forrest, M., Li, F., Melton, J. R., Yue, C., Archibald, S., Scheiter, S., Arneth, A., Hickler, T., and Sitch, S.: Global ecosystems and fire: Multi-model assessment of fire-induced tree-cover and carbon storage reduction, Global Change Biology, 26, 5027–5041, doi:10.1111/gcb.15160, 2020.

Lawrence, D. M., Fisher, R. A., Koven, C. D., Oleson, K. W., Swenson, S. C., Bonan, G., Collier, N., Ghimire, B., Kampenhout, L., Kennedy, D., Kluzek, E., Lawrence, P. J., Li, F., Li, H., Lombardozzi, D., Riley, W. J., Sacks, W. J., Shi, M., Vertenstein, M., Wieder, W. R., Xu, C., Ali, A. A., Badger, A. M., Bisht, G., Broeke, M., Brunke, M. A., Burns, S. P., Buzan, J., Clark, M., Craig, A., Dahlin, K., Drewniak, B., Fisher, J. B., Flanner, M., Fox, A. M., Gentine, P., Hoffman, F., Keppel-Aleks, G., Knox, R., Kumar, S., Lenaerts, J., Leung, L. R., Lipscomb, W. H., Lu, Y., Pandey, A., Pelletier, J. D., Perket, J., Randerson, J. T., Ricciuto, D. M., Sanderson, B. M., Slater, A., Subin, Z. M., Tang, J., Thomas, R. Q., Val Martin, M., and Zeng, X.: The Community Land Model Version 5: Description of New Features, Benchmarking, and Impact of Forcing Uncertainty, J. Adv. Model. Earth Syst., 11, 4245–4287, doi:10.1029/2018MS001583, 2019.

Le Quéré, C., Andres, R. J., Boden, T., Conway, T., Houghton, R. A., House, J. I., Marland, G., Peters, G. P., van der Werf, G. R., Ahlström, A., Andrew, R. M., Bopp, L., Canadell, J. G., Ciais, P., Doney, S. C., Enright, C., Friedlingstein, P., Huntingford, C., Jain, A. K., Jourdain, C., Kato, E., Keeling, R. F., Klein Goldewijk, K., Levis, S., Levy, P., Lomas, M., Poulter, B., Raupach, M. R., Schwinger, J., Sitch, S., Stocker, B. D., Viovy, N., Zaehle, S., and Zeng, N.: The global carbon budget 1959–2011, Earth Syst. Sci. Data, 5, 165–185, doi:10.5194/essd-5-165-2013, 2013.

Li, X., Xiao, J., He, B., Altaf Arain, M., Beringer, J., Desai, A. R., Emmel, C., Hollinger, D. Y., Krasnova, A., Mammarella, I., Noe, S. M., Ortiz, P. S., Rey-Sanchez, A. C., Rocha, A. V., and Varlagin, A.: Solar-induced chlorophyll fluorescence is strongly correlated with terrestrial photosynthesis for a wide variety of biomes: First global analysis based on OCO-2 and flux tower observations, Global Change Biology, 24, 3990–4008, doi:10.1111/gcb.14297, 2018.

Lienert, S. and Joos, F.: A Bayesian ensemble data assimilation to constrain model parameters and land-use carbon emissions, Biogeosciences, 15, 2909–2930, doi:10.5194/bg-15-2909-2018, 2018.

MacBean, N., Scott, R. L., Biederman, J. A., Peylin, P., Kolb, T., Litvak, M. E., Krishnan, P., Meyers, T. P., Arora, V. K., Bastrikov, V., Goll, D., Lombardozzi, D. L., Nabel, Julia E. M. S., Pongratz, J., Sitch, S., Walker, A. P., Zaehle, S., and Moore, D. J. P.: Dynamic global vegetation models underestimate net CO_2 flux mean and inter-annual variability in dryland ecosystems, Environ. Res. Lett., 16, 94023, doi:10.1088/1748-9326/ac1a38, 2021.

Masarie, K. A., Peters, W., Jacobson, A. R., and Tans, P. P.: ObsPack: a framework for the preparation, delivery, and attribution of atmospheric greenhouse gas measurements, Earth Syst. Sci. Data, 6, 375–384, doi:10.5194/essd-6-375-2014, 2014.

885 Meiyappan, P., Jain, A. K., and House, J. I.: Increased influence of nitrogen limitation on CO_2 emissions from future land use and land use change, Global Biogeochem. Cycles, 29, 1524–1548, doi:10.1002/2015GB005086, 2015.

Melton, J. R., Arora, V. K., Wisernig-Cojoc, E., Seiler, C., Fortier, M., Chan, E., and Teckentrup, L.: CLASSIC v1.0: the open-source community successor to the Canadian Land Surface Scheme (CLASS) and the Canadian Terrestrial Ecosystem Model (CTEM) – Part 1: Model framework and site-level performance, Geosci. Model Dev., 13, 2825–2850,
890 doi:10.5194/gmd-13-2825-2020, 2020.

Mengistu, A. G. and Mengistu Tsidu, G.: On the performance of satellite-based observations of XCO_2 in capturing the NOAA Carbon Tracker model and ground-based flask observations over Africa's land mass, Atmos. Meas. Tech., 13, 4009–4033, doi:10.5194/amt-13-4009-2020, 2020.

Metz, E.-M., Vardag, S. N., Basu, S., Jung, M., Ahrens, B., El-Madany, T., Sitch, S., Arora, V. K., Briggs, P. R.,
895 Friedlingstein, P., Goll, D. S., Jain, A. K., Kato, E., Lombardozzi, D., Nabel, Julia E. M. S., Poulter, B., Séférian, R., Tian, H., Wiltshire, A., Yuan, W., Yue, X., Zaehle, S., Deutscher, N. M., Griffith, D. W. T., and Butz, A.: Soil respiration-driven CO_2 pulses dominate Australia's flux variability, Science, 379, 1332–1335, doi:10.1126/science.add7833, 2023.

Muñoz Sabater, J.: ERA5-Land monthly averaged data from 1981 to present, Copernicus Climate Change Service (C3S)
900 Climate Data Store (CDS) [data set], doi:10.24381/cds.68d2bb3, 2019.

Muñoz Sabater, J.: ERA5-Land monthly averaged data from 1981 to present, Copernicus Climate Change Service (C3S) Climate Data Store (CDS) [data set], doi:10.24381/cds.68d2bb3, 2021.

OCO-2 Science Team, Gunson M., Eldering A.,,: ACOS GOSAT/TANSO-FTS Level 2 bias-corrected XCO2 and other select fields from the full-physics retrieval aggregated as daily files V9r, Greenbelt, MD, USA, Goddard Earth Sciences
905 Data and Information Services Center (GES DISC) [data set], https://doi.org/10.5067/VWSABTO7ZII4, 2019.

OCO-2/OCO-3 Science Team, Payne, V., Chatterjee, A.: OCO-2 Level 2 geolocatedbias-corrected XCO2 retrievals results, physical modeland other select fields from the full-physics retrieval aggregated as daily files, Retrospective Processing V11rprocessing V11.1r, Greenbelt, MD, USA, Goddard Earth Sciences Data and Information Services Center (GES DISC) [data set], https://doi.org/10.5067/8Z3QQKHC4R4C, 2020/10.5067/8E4VLCK16O6Q, 2022.

910 Pandey, S., Miller, J. B., Basu, S., Liu, J., Weir, B., Byrne, B., Chevallier, F., Bowman, K. W., Liu, Z., Deng, F., O'Dell, C. W., and Chatterjee, A.: Toward low-latency estimation of atmospheric CO2 growth rates using satellite observations: Evaluating sampling errors of satellite and in situ observing approaches. AGU Advances, 5, e2023AV001145, doi:10.1029/2023AV001145, 2024.

Pan, S., Yang, J., Tian, H., Shi, H., Chang, J., Ciais, P., Francois, L., Frieler, K., Fu, B., Hickler, T., Ito, A., Nishina, K.,
915 Ostberg, S., Reyer, C. P., Schaphoff, S., Steinkamp, J., and Zhao, F.: Climate Extreme Versus Carbon Extreme: Responses of Terrestrial Carbon Fluxes to Temperature and Precipitation, J. Geophys. Res. Biogeosci., 125, doi:10.1029/2019JG005252, 2020.

Peters, W., Jacobson, A. R., Sweeney, C., Andrews, A. E., Conway, T. J., Masarie, K., Miller, J. B., Bruhwiler, L. M. P., Pétron, G., Hirsch, A. I., Worthy, D. E. J., van der Werf, G. R., Randerson, J. T., Wennberg, P. O., Krol, M. C., and Tans, P. P.: An atmospheric perspective on North American carbon dioxide exchange: CarbonTracker, Proc. Natl. Acad. Sci. USA, 104, 18925–18930, doi:10.1073/pnas.0708986104, 2007.

Piao, S., Wang, X., Wang, K., Li, X., Bastos, A., Canadell, J. G., Ciais, P., Friedlingstein, P., and Sitch, S.: Interannual variation of terrestrial carbon cycle: Issues and perspectives, Glob Change Biol, 26, 300–318, doi:10.1111/gcb.14884, 2020.

Pierrat, Z., Magney, T., Parazoo, N. C., Grossmann, K., Bowling, D. R., Seibt, U., Johnson, B., Helgason, W., Barr, A., Bortnik, J., Norton, A., Maguire, A., Frankenberg, C., and Stutz, J.: Diurnal and Seasonal Dynamics of Solar-Induced Chlorophyll Fluorescence, Vegetation Indices, and Gross Primary Productivity in the Boreal Forest, J. Geophys. Res. Biogeosci., 127, doi:10.1029/2021JG006588, 2022.

Poulter, B., Ciais, P., Hodson, E., Lischke, H., Maignan, F., Plummer, S., and Zimmermann, N. E.: Plant functional type mapping for earth system models, Geosci. Model Dev., 4, 993–1010, doi:10.5194/gmd-4-993-2011, 2011.

Poulter, B., Frank, D., Ciais, P., Myneni, R. B., Andela, N., Bi, J., Broquet, G., Canadell, J. G., Chevallier, F., Liu, Y. Y., Running, S. W., Sitch, S., and van der Werf, G. R.: Contribution of semi-arid ecosystems to interannual variability of the global carbon cycle, Nature, 509, 600–603, doi:10.1038/nature13376, 2014.

Ramo, R., Roteta, E., Bistinas, I., van Wees, D., Bastarrika, A., Chuvieco, E., and van der Werf, G. R.: African burned area and fire carbon emissions are strongly impacted by small fires undetected by coarse resolution satellite data, Proceedings of the National Academy of Sciences of the United States of America, 118, doi:10.1073/pnas.2011160118, 2021.

Randerson, J. T., Thompson, M. V., Malmstrom, C. M., Field, C. B., and Fung, I. Y.: Substrate limitations for heterotrophs: Implications for models that estimate the seasonal cycle of atmospheric CO 2, Global Biogeochem. Cycles, 10, 585–602, doi:10.1029/96GB01981, 1996.

Reick, C. H., Gayler, V., Goll, D., Hagemann, S., Heidkamp, M., Nabel, Julia E. M. S., Raddatz, T., Roeckner, E., Schnur, R., and Wilkenskjeld, S.: JSBACH 3 - The land component of the MPI Earth System Model: documentation of version 3.2, Reports on Earth System Science, n/a-n/a, doi:10.17617/2.3279802, 2021.

Sellar, A. A., Jones, C. G., Mulcahy, J. P., Tang, Y., Yool, A., Wiltshire, A., O'connor, F. M., Stringer, M., Hill, R., Palmieri, J., and others: UKESM1: Description and evaluation of the UK Earth System Model, J. Adv. Model. Earth Syst., 11, 4513–4558, 2019.

Sellers, P. J., Schimel, D. S., Moore, B., Liu, J., and Eldering, A.: Observing carbon cycle–climate feedbacks from space, Proc. Natl. Acad. Sci. USA, 115, 7860–7868, doi:10.1073/pnas.1716613115, 2018.

Shi, Y., Matsunaga, T., Saito, M., Yamaguchi, Y., and Chen, X.: Comparison of global inventories of CO_2 emissions from biomass burning during 2002-2011 derived from multiple satellite products, Environmental pollution (Barking, Essex 1987), 206, 479–487, doi:10.1016/j.envpol.2015.08.009, 2015.

Steiner, A. L.: Role of the Terrestrial Biosphere in Atmospheric Chemistry and Climate, Accounts of chemical research, 53, 1260–1268, doi:10.1021/acs.accounts.0c00116, 2020.

Sun, Y., Frankenberg, C., Jung, M., Joiner, J., Guanter, L., Köhler, P., and Magney, T.: Overview of Solar-Induced chlorophyll Fluorescence (SIF) from the Orbiting Carbon Observatory-2: Retrieval, cross-mission comparison, and global monitoring for GPP, Remote Sensing of Environment, 209, 808–823, doi:10.1016/j.rse.2018.02.016, 2018.

Taylor, T. E., O'Dell, C. W., Crisp, D., Kuze, A., Lindqvist, H., Wennberg, P. O., Chatterjee, A., Gunson, M., Eldering, A., Fisher, B., Kiel, M., Nelson, R. R., Merrelli, A., Osterman, G., Chevallier, F., Palmer, P. I., Feng, L., Deutscher, N. M., Dubey, M. K., Feist, D. G., García, O. E., Griffith, D. W. T., Hase, F., Iraci, L. T., Kivi, R., Liu, C., Mazière, M. de, Morino, I., Notholt, J., Oh, Y.-S., Ohyama, H., Pollard, D. F., Rettinger, M., Schneider, M., Roehl, C. M., Sha, M. K., Shiomi, K., Strong, K., Sussmann, R., Té, Y., Velazco, V. A., Vrekoussis, M., Warneke, T., and Wunch, D.: An 11-year record of XCO$_2$ estimates derived from GOSAT measurements using the NASA ACOS version 9 retrieval algorithm, Earth Syst. Sci. Data, 14, 325–360, doi:10.5194/essd-14-325-2022, 2022.

Taylor, T. E., O'Dell, C. W., Baker, D., Bruegge, C., Chang, A., Chapsky, L., Chatterjee, A., Cheng, C., Chevallier, F., Crisp, D., Dang, L., Drouin, B., Eldering, A., Feng, L., Fisher, B., Fu, D., Gunson, M., Haemmerle, V., Keller, G. R., Kiel, M., Le Kuai, Kurosu, T., Lambert, A., Laughner, J., Lee, R., Liu, J., Mandrake, L., Marchetti, Y., McGarragh, G., Merrelli, A., Nelson, R. R., Osterman, G., Oyafuso, F., Palmer, P. I., Payne, V. H., Rosenberg, R., Somkuti, P., Spiers, G., To, C., Weir, B., Wennberg, P. O., Yu, S., and Zong, J.: Evaluating the consistency between OCO-2 and OCO-3 XCO 2 estimates derived from the NASA ACOS version 10 retrieval algorithm, Atmos. Meas. Tech., 16, 3173–3209, doi:10.5194/amt-16-3173-2023, 2023.

Tian, H., Chen, G., Lu, C., Xu, X., Hayes, D. J., Ren, W., Pan, S., Huntzinger, D. N., and Wofsy, S. C.: North American terrestrial CO2 uptake largely offset by CH4 and N2O emissions: toward a full accounting of the greenhouse gas budget, Climatic change, 129, 413–426, doi:10.1007/s10584-014-1072-9, 2015.

Tramontana, G., Jung, M., Schwalm, C. R., Ichii, K., Camps-Valls, G., Ráduly, B., Reichstein, M., Arain, M. A., Cescatti, A., Kiely, G., Merbold, L., Serrano-Ortiz, P., Sickert, S., Wolf, S., and Papale, D.: Predicting carbon dioxide and energy fluxes across global FLUXNET sites with regression algorithms, Biogeosciences, 13, 4291–4313, doi:10.5194/bg-13-4291-2016, 2016.

Valentini, R., Arneth, A., Bombelli, A., Castaldi, S., Cazzolla Gatti, R., Chevallier, F., Ciais, P., Grieco, E., Hartmann, J., Henry, M., Houghton, R. A., Jung, M., Kutsch, W. L., Malhi, Y., Mayorga, E., Merbold, L., Murray-Tortarolo, G., Papale, D., Peylin, P., Poulter, B., Raymond, P. A., Santini, M., Sitch, S., Vaglio Laurin, G., van der Werf, G. R., Williams, C. A., and Scholes, R. J.: A full greenhouse gases budget of Africa: synthesis, uncertainties, and vulnerabilities, Biogeosciences, 11, 381–407, doi:10.5194/bg-11-381-2014, 2014.

van der Velde, I. R., van der Werf, G. R., van Wees, D., Schutgens, N. A. J., Vernooij, R., Houweling, S., Tonucci, E., Chuvieco, E., Randerson, J. T., Frey, M. M., Borsdorff, T., and Aben, I.: Small Fires, Big Impact: Evaluating Fire

Emission Estimates in Southern Africa Using New Satellite Imagery of Burned Area and Carbon Monoxide, Geophys. Res. Lett., 51, doi:10.1029/2023GL106122, 2024.

van der Werf, G. R., Randerson, J. T., Giglio, L., van Leeuwen, T. T., Chen, Y., Rogers, B. M., Mu, M., van Marle, M. J. E., Morton, D. C., COLLATZ, G. J., Yokelson, R. J., and Kasibhatla, P. S.: Global fire emissions estimates during 1997–2016, Earth Syst. Sci. Data, 9, 697–720, doi:10.5194/essd-9-697-2017, 2017.

van Marle, M. J. E., Kloster, S., Magi, B. I., Marlon, J. R., Daniau, A.-L., Field, R. D., Arneth, A., Forrest, M., Hantson, S., Kehrwald, N. M., Knorr, W., Lasslop, G., Li, F., Mangeon, S., Yue, C., Kaiser, J. W., and van der Werf, G. R.: Historic global biomass burning emissions for CMIP6 (BB4CMIP) based on merging satellite observations with proxies and fire models (1750–2015), Geosci. Model Dev., 10, 3329–3357, doi:10.5194/gmd-10-3329-2017, 2017.

Vuichard, N., Messina, P., Luyssaert, S., Guenet, B., Zaehle, S., Ghattas, J., Bastrikov, V., and Peylin, P.: Accounting for carbon and nitrogen interactions in the global terrestrial ecosystem model ORCHIDEE (trunk version, rev 4999): multi-scale evaluation of gross primary production, Geosci. Model Dev., 12, 4751–4779, doi:10.5194/gmd-12-4751-2019, 2019.

Walker, A. P., Quaife, T., van Bodegom, P. M., Kauwe, M. G. de, Keenan, T. F., Joiner, J., Lomas, M. R., MacBean, N., Xu, C., Yang, X., and Woodward, F. I.: The impact of alternative trait-scaling hypotheses for the maximum photosynthetic carboxylation rate (Vcmax) on global gross primary production, The New phytologist, 215, 1370–1386, doi:10.1111/nph.14623, 2017.

Weber, U., Jung, M., Reichstein, M., Beer, C., Braakhekke, M. C., Lehsten, V., Ghent, D., Kaduk, J., Viovy, N., Ciais, P., Gobron, N., and Rödenbeck, C.: The interannual variability of Africa's ecosystem productivity: a multi-model analysis, Biogeosciences, 6, 285–295, doi:10.5194/bg-6-285-2009, 2009.

Weir, B., Ott, L. E., Collatz, G. J., Kawa, S. R., Poulter, B., Chatterjee, A., Oda, T., and Pawson, S.: Bias-correcting carbon fluxes derived from land-surface satellite data for retrospective and near-real-time assimilation systems, Atmos. Chem. Phys., 21, 9609–9628, doi:10.5194/acp-21-9609-2021, 2021.

Wiedinmyer, C., Akagi, S. K., Yokelson, R. J., Emmons, L. K., Al-Saadi, J. A., Orlando, J. J., and Soja, A. J.: The Fire INventory from NCAR (FINN) – a high resolution global model to estimate the emissions from open burning, Geosci. Model Dev., 4, 625–641, doi:10.5194/gmdd-3-2439-2010, 2011.

Williams, C. A., Hanan, N. P., Baker, I., COLLATZ, G. J., Berry, J., and Denning, A. S.: Interannual variability of photosynthesis across Africa and its attribution, J. Geophys. Res., 113, doi:10.1029/2008JG000718, 2008.

Williams, C. A., Hanan, N. P., Neff, J. C., Scholes, R. J., Berry, J. A., Denning, A. S., and Baker, D. F.: Africa and the global carbon cycle, Carbon balance and management, 2, 3, doi:10.1186/1750-0680-2-3, 2007.

Wunch, D., Toon, G. C., Blavier, J.-F. L., Washenfelder, R. A., Notholt, J., Connor, B. J., Griffith, D. W. T., Sherlock, V., and Wennberg, P. O.: The Total Carbon Column Observing Network, Phil. Trans. R. Soc. A., 369, 2087–2112, doi:10.1098/rsta.2010.0240, 2011.

Yuan, W., Liu, D., Dong, W., Liu, S., Zhou, G., Yu, G., Zhao, T., Feng, J., Ma, Z., Chen, J., Chen, Y., Chen, S., Han, S., Huang, J., Li, L., Liu, H., Liu, S., Ma, M., Wang, Y., Xia, J., Xu, W., Zhang, Q., Zhao, X., and Zhao, L.: Multiyear precipitation reduction strongly decreases carbon uptake over northern China, J. Geophys. Res. Biogeosci., 119, 881–896, doi:10.1002/2014JG002608, 2014.

Yue, X. and Unger, N.: The Yale Interactive terrestrial Biosphere model version 1.0: description, evaluation and implementation into NASA GISS ModelE2, Geosci. Model Dev., 8, 2399–2417, doi:10.5194/gmd-8-2399-2015, 2015.

Zaehle, S., Friend, A. D., Friedlingstein, P., Dentener, F., Peylin, P., and Schulz, M.: Carbon and nitrogen cycle dynamics in the O-CN land surface model: 2. Role of the nitrogen cycle in the historical terrestrial carbon balance, Global Biogeochem. Cycles, 24, n/a-n/a, doi:10.1029/2009GB003522, 2010.

Zeng, N., Mariotti, A., and Wetzel, P.: Terrestrial mechanisms of interannual CO 2 variability, Global Biogeochem. Cycles, 19, doi:10.1029/2004gb002273, 2005.

Zhang, X., Wang, Y.-P., Peng, S., Rayner, P. J., Ciais, P., Silver, J. D., Piao, S., Zhu, Z., Lu, X., and Zheng, X.: Dominant regions and drivers of the variability of the global land carbon sink across timescales, Global Change Biology, 24, 3954–3968, doi:10.1111/gcb.14275, 2018.

Zhang, Y., Guanter, L., Berry, J. A., van der Tol, C., Yang, X., Tang, J., and Zhang, F.: Model-based analysis of the relationship between sun-induced chlorophyll fluorescence and gross primary production for remote sensing applications, Remote Sensing of Environment, 187, 145–155, doi:10.1016/j.rse.2016.10.016, 2016a.

Zhang, Y., Xiao, X., Jin, C., Dong, J., Zhou, S., Wagle, P., Joiner, J., Guanter, L., Zhang, Y., Zhang, G., Qin, Y., Wang, J., and Moore, B.: Consistency between sun-induced chlorophyll fluorescence and gross primary production of vegetation in North America, Remote Sensing of Environment, 183, 154–169, doi:10.1016/j.rse.2016.05.015, 2016b.